

A COMPARISON BETWEEN SEMI-ANALYTIC MODEL PREDICTIONS FOR THE CANDELS SURVEY

YU LU¹, RISA H. WECHSLER¹, RACHEL S. SOMERVILLE², DARREN CROTON³, LAUREN PORTER⁴, JOEL PRIMACK⁴, PETER S. BEHROOZI⁵, HENRY C. FERGUSON⁵, DAVID C. KOO⁶, YICHENG GUO⁶, MOHAMMADTAHER SAFARZADEH⁷, KRISTIAN FINLATOR⁸, MARCO CASTELLANO⁹, CATHERINE E. WHITE⁷, VERONICA SOMMARIVA⁹, CHRIS MOODY⁴

Draft version July 11, 2018

ABSTRACT

We compare the predictions of three independently developed semi-analytic galaxy formation models (SAMs) that are being used to aid in the interpretation of results from the CANDELS survey. These models are each applied to the same set of halo merger trees extracted from the “Bolshoi” high-resolution cosmological N -body simulation and are carefully tuned to match the local galaxy stellar mass function using the powerful method of Bayesian Inference coupled with Markov Chain Monte Carlo (MCMC) or by hand. The comparisons reveal that in spite of the significantly different parameterizations for star formation and feedback processes, the three models yield qualitatively similar predictions for the assembly histories of galaxy stellar mass and star formation over cosmic time. Comparing SAM predictions with existing estimates of the stellar mass function from $z = 0 - 8$, we show that the SAMs generally require strong outflows to suppress star formation in low-mass halos to match the present day stellar mass function, as is the present common wisdom. However, all of the models considered produce predictions for the star formation rates and metallicities of low-mass galaxies that are inconsistent with existing data. The predictions for metallicity-stellar mass relations and their evolution clearly diverge between the models. We suggest that large differences in the metallicity relations and small differences in the stellar mass assembly histories of model galaxies stem from different assumptions for the outflow mass-loading factor produced by feedback. Importantly, while more accurate observational measurements for stellar mass, star formation rate and metallicity of galaxies at $1 < z < 5$ will discriminate between models, the discrepancies between the constrained models and existing data of these observables have already revealed challenging problems in understanding star formation and its feedback in galaxy formation. The three sets of models are being used to construct catalogs of mock galaxies on light cones that have the same geometry as the CANDELS survey, which should be particularly useful for quantifying the biases and uncertainties on measurements and inferences from the real observations.

1. INTRODUCTION

Over the past three decades, a number of theoretical methods have been developed to study the formation and evolution of galaxies. Among these, semi-analytic models (SAMs) have become a widely used tool to study the formation and evolution of galaxies in a cosmological context, owing to their relatively light computational demands and great flexibility for exploring the effects of different physical assumptions.

SAMs follow astrophysical processes affecting the baryonic components of galaxies using simple, yet physically, and/or empirically motivated recipes. In those recipes, the evolution of each baryonic component is followed by a set of differential equations that track the mass of each component as a function of time, depending on other properties (e.g. halo mass and angular momentum, gas mass, metallicity, etc). The models are embedded either in Monte Carlo realizations of an analytic representation of dark matter halo formation histories (White & Frenk 1991; Kauffmann et al. 1993; Cole et al. 1994; Somerville & Kolatt 1999) or in a direct numerical simulation (Kauffmann et al. 1999; Springel et al. 2001; Springel et al. 2005) of the evolution of the underlying dark matter distribution. The pioneering work by White & Rees (1978) first laid the theoretical groundwork for this type of model and more detailed processes started to be included in the 1990s (Cole 1991; White & Frenk 1991; Kauffmann et al. 1993; Somerville & Primack 1999). Over the past ten years, such models have been substantially extended and refined by a number of different groups (for reviews, see Baugh 2006; Benson 2012). SAMs can yield a rich set of predictions for the evolution of various galaxy properties, such as the distributions of stellar mass, luminosity, star formation rate, size, rotation velocity, morphology, gas content, and metallicity, as well as the scaling relations linking these properties.

¹Kavli Institute for Particle Astrophysics & Cosmology, Physics Department, and SLAC National Accelerator Laboratory, Stanford University, Stanford, CA 94305
luyu@stanford.edu, rwechsler@stanford.edu

²Department of Physics and Astronomy, Rutgers University, 136 Frelinghuysen Road, Piscataway, NJ 08854, USA

³Centre for Astrophysics & Supercomputing, Swinburne University of Technology, PO Box 218, Hawthorn, VIC 3122, Australia

⁴Department of Physics, University of California at Santa Cruz, Santa Cruz, CA 95064, USA

⁵Space Telescope Science Institute, 3700 San Martin Drive, Baltimore, MD 21218, USA

⁶UCO/Lick Observatory, Department of Astronomy and Astrophysics, University of California, Santa Cruz, CA 95064, USA

⁷Department of Physics & Astronomy, The Johns Hopkins University, 3400 North Charles Street, Baltimore, MD 21218, USA

⁸Dark Cosmology Centre, Niels Bohr Institute, University of Copenhagen, Copenhagen, Denmark

⁹INAF - Osservatorio Astronomico di Roma, via Frascati 33, 00040, Monteporzio, Italy

Because the physical processes of galaxy formation are not well understood, SAMs generally have large uncertainties in their model parameterization and their choice of parameter values. A key goal of any semi-analytic model is to constrain these uncertainties using observational data and to better understand the processes through detailed calculations or simulations. Currently, such uncertainties are represented by adjustable parameters governing the efficiencies and scalings of these processes (note that this is true also for cosmological hydrodynamical simulations). Different groups typically adopt different parameterizations for modeling the processes and different values for those parameters. It is important to understand the impact of these model recipes and their parameters on the predicted galaxy properties.

After a SAM is developed or significantly updated, a new paper is generally written to report on how the model is tuned to match observational data, and to make new predictions for various observables (e.g. Bower et al. 2006; Cattaneo et al. 2006; Croton et al. 2006; Menci et al. 2006; De Lucia & Blaizot 2007; Monaco et al. 2007; Somerville et al. 2008; Guo et al. 2011). However, to date there have been only a few direct comparisons between different semi-analytic model codes. One approach is to compare the recipes adopted by various groups by implementing them as modules within a single code, as in an early study by Somerville & Primack (1999) and more recently in Lu et al. (2011a). Other studies have compared models that are based on different merger trees, and for which no attempt has been made to normalize the models in the same way (Fontanot et al. 2009; Kimm et al. 2009). Similarly, Wang et al. (2012) and Weinmann et al. (2012) took models by Guo et al. (2011) and Neistein & Weinmann (2010) with varied parameters to understand the effect of the star formation and SN feedback. Macciò et al. (2010) compared three different SAMs run in the same merger trees, but focused only on Milky Way mass halos. De Lucia et al. (2010) presented a comparison of three different SAMs run within the same merger trees, but for “stripped down” versions of the SAMs that contained only cooling and merging.

The above studies have shown that the model predictions are sensitive to some of the model parameters, while other parameters are degenerate. Furthermore, models based on very different parameterizations can make similar predictions for some observables, which suggests that those predictions are insensitive to the choice of model recipes (i.e. how the physics itself is implemented). In this paper, we compare model predictions from three independently developed semi-analytic models, namely the Croton model (Croton et al. 2006, Croton et al. in prep) the Somerville model (Somerville et al. 2008, 2012) and the Lu model (Lu et al. 2011b). Our goal is to understand the impact of the different model assumptions on the predicted observables when the different models are applied to the same underlying merger trees and are carefully tuned to match some basic observational constraints. The present paper focuses on the most fundamental physical properties, e.g. stellar mass, star formation rate (SFR), stellar and cold gas metallicities, cold gas mass, etc, predicted by the models in this large comparison.

All the models presented in this paper are being used to produce mock catalogs for the Cosmic Assembly Near-IR Deep Extragalactic Legacy Survey (CANDELS Koekemoer et al. 2011; Grogin et al. 2011). CANDELS is an observational project that has just completed a three year run of data taking on the Hubble Space Telescope. The survey is designed to reveal the evolution of galaxies from their infancy to the present day via deep imaging of more than 250,000 galaxies with the new wide-field near-infrared camera (WFC3) installed on Hubble in 2009. A number of light cone realizations that mimic the geometry of the CANDELS fields are populated with galaxies using these three SAMs. The mock catalogs contain the most important physical properties of galaxies, such as stellar mass and star formation rate, as well as observables such as luminosities in all CANDELS bands. This paper thus also serves to present the basic properties predicted by the three models. Note that only a subset of the quantities in the present comparison can be directly measured by CANDELS. Those quantities are the most important ones for us to understand the similarities and differences between the models, i.e., the rate at which galaxies assemble their stellar mass, form their stars, and build up their metals. In a series of follow-up papers, we will investigate more directly observable quantities, i.e. magnitudes and colors, which depend on these underlying quantities and also on additional model assumptions, for example, the stellar population synthesis model and dust model. The comparisons of the most basic quantities in this paper will guide us in interpreting the results presented in future papers, as well as provide insights into how robust these predictions are to variations in the parameterization of physical recipes and their detailed implementation in different codes.

The paper is organized as follows. In Section 2, we describe the SAMs that are studied in the comparison. In Section 3, we summarize the merger trees on which all three SAMs are built, and the method we use to calibrate the models. We show the model predictions and comparisons in Section 4, and conclude our study in Section 5 with an overview of our key results. Throughout the paper, we use a Λ CDM cosmology with $\Omega_{M,0} = 0.27$, $\Omega_{\Lambda,0} = 0.73$, $\Omega_{b,0} = 0.044$, $h = 0.70$, $n = 0.95$, and $\sigma_8 = 0.82$. These values are adopted in the Bolshoi simulation (Klypin et al. 2011), and are consistent with the 7-year Wilkinson Microwave Anisotropy Probe (WMAP7) data (Jarosik et al. 2011) and the WMAP5 data (Dunkley et al. 2009; Komatsu et al. 2009)¹⁰. To focus our comparison on the different treatments of galaxy formation processes rather than stellar evolution models, we fix the initial mass function (IMF) to the Chabrier IMF (Chabrier 2003) with the stellar mass range of $0.1M_{\odot} < M < 100M_{\odot}$. In the comparisons between model predictions and observational data, the observationally derived stellar masses are converted by adopting the same IMF and are based on the BC03 stellar population synthesis model (Bruzual & Charlot 2003).

2. SEMI-ANALYTIC MODELS

¹⁰ The values used here are not fully consistent with the recent results from the Planck collaboration (Planck Collaboration et al. 2013), but our key results are largely insensitive to changes in the cosmological parameters at this level.

TABLE 1
SUMMARY OF MODEL RECIPES AND PARAMETER VALUES

process	Croton	Somerville	Lu ^a
re-ionization	Gnedin et al. 2000; Kravtsov et al. 2004	same	same
equation	Eq.2	Eq.2	Eq.2
parameters	$z_{\text{reion}} = 7, z_{\text{overlap}} = 8$	$z_{\text{reion}} = 11, z_{\text{overlap}} = 12$	$z_{\text{reion}} = 10, z_{\text{overlap}} = 11$
cooling	Croton et al. 2006	Croton et al. 2006, but assumes half of the hot gas accretes onto a central galaxy in a dynamical time when the cooling radius is larger than the virial radius to avoid the discontinuity in the cooling rate when $r_{\text{cool}} = R_{\text{vir}}$	Croton et al. 2006
star formation	only cold gas above a critical mass forms stars; constant star formation efficiency;	Schmidt-Kennicutt law; only cold gas above a threshold surface density forms stars;	only cold gas above a threshold surface density forms stars; efficiency depends on V_{vir} ;
equations	Eq. 7	Eq. 8, 11	Eq. 12, 15, 14
parameters	$\alpha_{\text{SF}} = 0.05$	$A_{\text{Kenn}} = 8.33 \times 10^{-9} M_{\odot} \text{yr}^{-1} \text{kpc}^{-2}, N_{\text{K}} = 1.4, \Sigma_{\text{crit}} = 6 M_{\odot} \text{pc}^{-2}$	$\alpha_{\text{SF}} \in [0.0056, 0.41], \beta_{\text{SF}} \in [0.05, 4.7], V_{\text{SF}} \in [32.4, 281] \text{km/s}, f_{\text{SF}} \in [0.11, 3.9]$
SN feedback	reheat cold gas, eject hot gas	reheat cold gas, eject cold gas	reheat cold gas, eject cold gas and hot gas
equations	Eq. 18, 21	Eq. 22; 23	Eq. 24, 23, 25
parameters	$\alpha_{\text{LD}} = 3.5, \alpha_{\text{SN}} = 0.35, \chi_{\text{ri}} = 0.5$	$\alpha_{\text{LD}} = 1.5, \beta_{\text{LD}} = 2.25, V_{\text{EJ}} = 130 \text{km/s}, \beta_{\text{EJ}} = 6$	$\alpha_{\text{LD}} \in [0.011, 1.1], \beta_{\text{LD}} \in [3.3, 9.9], V_{\text{EJ}} \in [35, 970] \text{km/s}, \beta_{\text{EJ}} \in [0.08, 7.7], \alpha_{\text{SN}} \in [0.016, 9.3], \epsilon_{\text{W}} \in [0.0011, 0.71], \chi_{\text{ri}} \in [0.01, 0.66]$
quenching model	radio mode and quasar mode	radio mode and quasar mode	halo quenching
equations	Eq. 27, 26, 28	Eq. 34, 35, 36	
parameters	$f_{\text{BH}} = 0.015, \kappa_{\text{AGN}} = 1 \times 10^{-3} M_{\odot} / \text{yr}, \eta_{\text{AGN}} = 0.005$	$\sigma_{\text{BH}} = 0.3, f_{\text{BH,FINAL}} = 2, \kappa_{\text{radio}} = 4.3 \times 10^{-3}, \kappa_{\text{heat}} = 1, \eta_{\text{rad}} = 0.1, \epsilon_{\text{wind}} = 0.5$	$M_{\text{cc}} \in [10^{11}, 10^{12.1}] M_{\odot} / h, \sigma_{\text{CC}} \in [0.064, 1.1]$
starburst	when two galaxies merge; efficiency depends on the baryonic mass ratio	when two galaxies merge; efficiency depends on the mass ratio and the gas fraction	when two galaxies merge; efficiency depends on the mass ratio
equations	Eq. 38	Eq. 7-10 in Somerville et al. (2008)	Eq. 38
parameters	$\alpha_{\text{burst}} = 0.56, \beta_{\text{burst}} = 0.73$	$\epsilon_{\text{burst}}, \tau_{\text{burst}}$	$\alpha_{\text{burst}} = 0.56, \beta_{\text{burst}} = 0.73$
satellite kinematics	subhalo info from simulation; dynamical friction model is used to determine whether a satellite is stripped or merged with a central galaxy	dynamical friction model (Boylan-Kolchin et al. 2008)	subhalo info from simulation and dynamical friction when subhalo is unresolved
equation	Eq. 37	Eq. 39	Eq. 42
parameters			$f_{\text{DF}} \in [1.6, 91.6]$
satellite stripping	hot gas is stripped in proportion to the subhalo dark matter mass stripping; the entire satellite galaxy is stripped or merged with a central galaxy when a subhalo mass is reduced below a certain halo mass to galaxy mass ratio	hot gas is instantaneously stripped when a halo enters the virial radius of a bigger halo; the entire stellar and cold gas mass is instantaneously stripped when the galaxy is considered tidally disrupted	hot gas is instantaneously stripped when a halo becomes a subhalo; the cold gas is instantaneously stripped when a subhalo loses its identity in the merger tree; a fraction of stellar mass is stripped in every orbital timescale after the subhalo is lost
equation			
parameters	$f_{\text{ST,crit}} = 2$	$f_{\text{strip}} = 1, f_{\text{dis}} = 1$	$f_{\text{ST}} = [0.11, 0.98]$

^aFor the Lu model, numbers in the parentheses encompass 95% posterior range of the free parameters in the model.

Throughout this paper we use the Croton model (Croton et al. 2006, Croton et al. in prep) (also known as the Semi-Analytic Galaxy Evolution, or SAGE, model), the Somerville model (Somerville et al. 2008), and the Lu model (Lu et al. 2011b). Below we review the implementations and parameterizations of the most important processes included in each model. These processes include re-ionization (§2.2), radiative cooling (§2.3), ‘normal’ star formation in galaxy disks (§2.4), supernova (SN) feedback (§2.5), AGN feedback and halo quenching (§2.6), galaxy-galaxy mergers (§2.7), and chemical

evolution (§2.8).

2.1. Baryonic matter budget

In a SAM, every dark matter halo hosts a number of baryonic matter components. A typical SAM contains hot gas, cold gas, stellar mass in a bulge and disk component, ejected gas, and black hole mass. The basic task of a SAM is to follow the evolution of the mass in these components.

It is normally assumed that every dark matter halo can acquire a baryonic mass totaling $f_b M_{\text{vir}}$, where $f_b = \Omega_b / \Omega_0$ is the universal baryon fraction, and M_{vir} is the

virial mass of the dark matter halo. The physical processes assumed in the model can, however, change the total amount of baryonic matter by preventing baryons from accreting onto the halo or ejecting the accreted baryons out of the halo. In the models adopted here, we assume that at every timestep as we follow the assembly of a dark matter halo, a halo accretes some stellar mass, cold gas and/or black hole mass, which has formed in its progenitor halos. Sometimes a galaxy merges with another galaxy, at which time the corresponding components in merger progenitors are combined together and may trigger a starburst.

In addition to the cold gas in a galaxy disk, the models also assume that a certain baryonic mass is accreted into the halo as a diffuse hot gas component. The total mass of hot halo gas is

$$M_{\text{hot}} = f_{\text{b,coll}} f_{\text{b}} M_{\text{vir}} - \sum_i [M_{*,i} + M_{\text{cold},i} + M_{\text{BH},i} + M_{\text{ej},i}], \quad (1)$$

where $f_{\text{b,coll}}$ is the baryon fraction that can accrete onto a halo limited by some physical processes (for example, re-ionization), M_* , M_{cold} , M_{BH} and M_{ej} are the masses in stars, cold gas, the supermassive black hole and ejected gas, respectively, and the summation is over all galaxies in the halo. In the rest of this section we describe the physical processes that transfer baryonic mass from one component to another and the parameterizations for these processes in the three different models.

2.2. Re-ionization

Gnedin (2000) showed that the fraction of baryons that can collapse into halos of a given mass in the presence of a photoionizing background can be described in terms of the ‘filtering mass’, M_{F} . Haloes less massive than M_{F} can confine less baryonic mass than the universal average. Gnedin (2000) parametrized the collapsed baryon fraction as a function of redshift and halo mass with the expression

$$f_{\text{b,coll}}(z, M_{\text{vir}}) = \frac{f_{\text{b}}}{[1 + 0.26 M_{\text{F}}(z)/M_{\text{vir}}]^3}, \quad (2)$$

where f_{b} is the universal baryon fraction and M_{vir} is the halo virial mass. The filtering mass is a function of redshift, and this function depends on the re-ionization history of the Universe. Kravtsov et al. (2004) provide a fitting formula for the filtering mass as a function of the redshift at which the first HII regions begin to overlap (z_{overlap}) and the redshift at which most of the medium is re-ionized (z_{reion}). Recent results from the WMAP experiment suggest an earlier epoch of re-ionization, $z_{\text{reion}} > 10$ (Spergel et al. 2007). All three of our models make use of the fitting functions (B2) and (B3) from appendix B of Kravtsov et al. (2004) to compute the initial fraction of baryons that can collapse as a function of halo mass and redshift, $f_{\text{b,coll}}$, with two parameters z_{overlap} and z_{reion} .

2.3. Radiative cooling: hot gas to cold gas

All three models follow the treatment of Croton et al. (2006), first introduced by Springel et al. (2001), to predict accretion and radiative cooling of hot gas. In the

model, the halo hot gas is redistributed in every time-step, and the density of the hot gas is assumed to have a singular isothermal profile,

$$\rho_{\text{hot}} = \frac{M_{\text{hot}}}{4\pi R_{\text{vir}}} r^{-2}, \quad (3)$$

where R_{vir} is the virial radius of the halo. The temperature of the hot gas, T_{hot} , is assumed to be a constant for each halo with $T_{\text{hot}} = 35.9 \left(\frac{V_{\text{vir}}}{\text{km s}^{-1}}\right)^2 \text{K}$, where V_{vir} is the circular velocity of the halo at the virial radius. The cooling timescale of the gas at radius r is then estimated by

$$\tau_{\text{cool}}(r) = \frac{3}{2} \frac{\mu m_{\text{H}} k T_{\text{hot}}}{\rho_{\text{hot}}(r) \Lambda(T_{\text{hot}}, Z_{\text{hot}})}, \quad (4)$$

where μ is the mean molecular weight in units of the mass of hydrogen atom, Λ is the cooling function from Sutherland & Dopita (1993), and Z_{hot} is the metallicity of the hot gas. At each timestep, each model calculates the cooling radius r_{cool} by equating the cooling timescale with the dynamical timescale of the host halo, $\tau_{\text{cool}} = \tau_{\text{dyn}} \equiv R_{\text{vir}}/V_{\text{vir}}$. If the cooling radius is equal to or smaller than the virial radius, the estimated cooling rate is

$$\dot{m}_{\text{cool}} = 0.5 M_{\text{hot}} \frac{r_{\text{cool}} V_{\text{vir}}}{r_{\text{vir}}^2}. \quad (5)$$

In other words, half of the hot gas mass enclosed by the cooling radius cools and accretes onto the central galaxy of the halo in a dynamical time. If the cooling radius is larger than the virial radius, the Croton and Lu models set the cooling rate to be equal to the total hot gas mass in the halo divided by the dynamical time, but the Somerville model sets the cooling rate to be half of the hot gas mass, rather than the total amount, divided by the dynamical time. The Lu model and the Somerville model implicitly assume that all hot gas is associated with the primary halo and only the central galaxy of the primary halo can accrete cooling gas; satellite galaxies, even if they have associated subhalos, do not accrete any hot gas.

Although this radiative cooling model does not have any explicit free parameters, this does not mean the theory for radiative cooling of halo gas is certain. Lu et al. (2011a) have explored various model recipes adopted in different SAMs and found that they predict cooling rates that differ from each other by a factor of 2 for low mass halos ($< 10^{12} M_{\odot}$), and even larger for more massive halos (also see Saro et al. 2010). In this paper, we fix the cooling recipe for all the models and focus our comparisons on the impact of other parts of the model related to the star formation and feedback processes.

2.4. Star formation: cold gas to stars

All three models assume that cooled gas settles into a disk in the central galaxy of a halo, but they adopt different prescriptions for the rate at which this gas turns into stars. In addition, each distinguishes between ‘normal’ star formation in the disk and merger-driven starbursts. We first describe disk star formation.

2.4.1. The Croton model

The Croton model assumes that cold gas is distributed in an exponential disk, and star formation is regulated by

a critical surface density (Kennicutt 1998), below which stars do not form. Practically, star formation occurs when the cold gas mass of the galaxy, M_{cold} , exceeds a critical mass, m_{crit} , suggested by the empirical relation of Kauffmann (1996)

$$m_{\text{crit}} = 3.8 \times 10^9 \left(\frac{V_{\text{vir}}}{200 \text{ km s}^{-1}} \right) \left(\frac{r_{\text{gas}}}{10 \text{ kpc}} \right) M_{\odot}, \quad (6)$$

where r_{gas} is the characteristic radius of the cold gas disk which is set to be three times larger than the stellar disk scale-length, r_s . Following the simplified model of Mo et al. (1998), where the density profile of the host halo is assumed to be a singular isothermal sphere and halo contraction is ignored, the model sets $r_s = (\lambda/\sqrt{2})R_{\text{vir}}$, where λ is the spin parameter of the host halo. The star formation rate of the galaxy, SFR , is then given by

$$SFR = \alpha_{\text{SF}} \frac{M_{\text{cold}} - m_{\text{crit}}}{\tau_{\text{disk}}}, \quad (7)$$

where $\tau_{\text{disk}} = r_{\text{gas}}/V_{\text{vir}}$ is the dynamical time of the gaseous disk and α_{SF} is a free parameter controlling the efficiency with which the cold gas is converted into stars over this timescale.

2.4.2. The Somerville model

The Somerville model also adopts a star formation recipe based on the empirical Schmidt-Kennicutt relation (Kennicutt 1989, 1998), but implemented in a somewhat different manner. Here, the star formation rate surface density of the disk is calculated according to

$$\Sigma_{\text{SFR}} = \begin{cases} A_{\text{Kenn}} \Sigma_{\text{gas}}^{N_{\text{K}}}, & \Sigma_{\text{gas}} > \Sigma_{\text{crit}}; \\ 0, & \text{otherwise.} \end{cases} \quad (8)$$

Here, $A_{\text{Kenn}} = 1.67 \times 10^{-4} M_{\odot} \text{ yr}^{-1} \text{ kpc}^{-2}$, $N_{\text{K}} = 1.4$ and Σ_{gas} is the surface density of cold gas in the disk in units of $M_{\odot} \text{ pc}^{-2}$, which are taken from the observationally derived values of Kennicutt (1998), converted to a Chabrier IMF. The gas distribution follows an exponential profile, with a characteristic radius $r_{\text{gas}} = 1.5r_s$, where r_s is calculated using the full model of Mo et al. (1998) with the assumption that the host halo has an NFW density profile and the halo mass distribution is contracted in response to the formation of a central galaxy in the halo center:

$$r_{\text{gas}} = \frac{1}{\sqrt{2}} f_j \lambda R_{\text{vir}} f_c^{-1/2} f_{\text{R}}(\lambda, c, f_{\text{d}}), \quad (9)$$

where $f_j \equiv (J_{\text{d}}/m_{\text{d}})/(J_{\text{h}}/M_{\text{vir}})$ is the ratio of the specific angular momentum of the disk and the halo, c is the concentration of the halo, and f_{d} is the disk mass to the halo mass ratio. Comparing with the Croton model, $f_c^{-1/2}$ reflects the difference in energy of a singular isothermal profile versus the NFW profile, and f_{R} reflects the adiabatic contraction of a NFW halo (see Mo et al. (1998) for expressions governing f_{R} and f_c).

The model assumes that only the gas above a critical surface density threshold Σ_{crit} ($= 6 M_{\odot} \text{ pc}^{-2}$) is available for star formation. The critical surface density gives a critical radius,

$$r_{\text{crit}} = -\ln \left[\frac{\Sigma_{\text{crit}}}{\Sigma_0} \right] r_{\text{gas}}, \quad (10)$$

where $\Sigma_0 = M_{\text{cold}}/(2\pi r_{\text{gas}}^2)$. The total star formation rate is then

$$SFR = 2\pi \int_0^{r_{\text{crit}}} \Sigma_{\text{SFR}}(r) r dr = \frac{2\pi A_{\text{Kenn}} \Sigma_0^{N_{\text{K}}} r_{\text{gas}}^2}{N_{\text{K}}^2} \times \left[1 - \left(1 + \frac{N_{\text{K}} r_{\text{crit}}}{r_{\text{gas}}} \right) \exp(-N_{\text{K}} r_{\text{crit}}/r_{\text{gas}}) \right]. \quad (11)$$

2.4.3. The Lu model

The Lu model also assumes that cold gas is distributed in an exponential disk with scale radius r_{gas} , and only gas mass with a surface density higher than a certain threshold, Σ_{crit} , can form stars (e.g. Kennicutt 1998; Kennicutt et al. 2007; Bigiel et al. 2008). The model assumes a fiducial value of the parameter for the threshold surface density of $\Sigma_{\text{crit},0} = 10 M_{\odot} \text{ pc}^{-2}$ but allows it to change in a range covering the observational uncertainty, $\Sigma_{\text{crit}} \sim 3 - 10 M_{\odot} \text{ pc}^{-2}$ (Schaye 2004, and references therein), by introducing a free parameter f_{SF} defined below. For simplicity, when calculating r_{gas} , the model adopts a single value $\lambda = 0.035$ for all halo spins. The fiducial size of the gaseous disk is then $r_{\text{gas},0} = \frac{0.035}{\sqrt{2}} R_{\text{vir}}$. The cold gas mass that has a surface density above a threshold surface density Σ_{crit} and is available for star formation is then

$$m_{\text{sf}} = M_{\text{cold}} \left[1 - \left[1 + \ln \left(\frac{\Sigma_{\text{cold},0}}{f_{\text{SF}} \Sigma_{\text{crit},0}} \right) \right] \frac{f_{\text{SF}} \Sigma_{\text{crit},0}}{\Sigma_{\text{cold},0}} \right], \quad (12)$$

where $\Sigma_{\text{cold},0} = M_{\text{cold}}/(2\pi r_{\text{gas},0}^2)$, and the model parameter f_{SF} is defined as

$$f_{\text{SF}} = \left(\frac{r_{\text{gas}}}{r_{\text{gas},0}} \right)^2 \left(\frac{\Sigma_{\text{crit}}}{\Sigma_{\text{crit},0}} \right). \quad (13)$$

The model parameter f_{SF} absorbs the uncertainties in both the size of the gaseous disk and the threshold surface density of the cold gas for star formation. As before, we take the star formation rate to be proportional to the mass of star forming gas and inversely proportional to the dynamical timescale of the disk, $\tau_{\text{disk}} = \frac{r_{\text{gas},0}}{V_{\text{vir}}}$, yielding

$$SFR = \epsilon_{\text{sf}} \frac{m_{\text{sf}}}{\tau_{\text{disk}}}, \quad (14)$$

where ϵ_{sf} governs star formation efficiency.

A variety of factors, such as small scale stellar feedback, turbulence, etc, could affect the timescale for the gas to be depleted by star formation, so to generalize this model for the star formation efficiency, the Lu model further assumes a halo circular velocity dependence for the star formation efficiency such that ϵ_{sf} has a broken power-law dependence on the circular velocity of the host halo (e.g. Cole et al. 1994; Kang et al. 2005):

$$\epsilon_{\text{sf}} = \begin{cases} \alpha_{\text{SF}} & V_{\text{vir}} \geq V_{\text{SF}}; \\ \alpha_{\text{SF}} \left(\frac{V_{\text{vir}}}{V_{\text{SF}}} \right)^{\beta_{\text{SF}}} & V_{\text{vir}} < V_{\text{SF}}, \end{cases} \quad (15)$$

where α_{SF} , β_{SF} and V_{SF} are model parameters in addition to f_{SF} .

2.5. SN feedback model: outflow and re-infall

With each new star formation episode, the high mass stars ($\gtrsim 8M_{\odot}$) will rapidly evolve and end their lives as energetic supernovae, on timescales much shorter than the time resolution of the models. The injection of this energy into the galaxy interstellar medium will heat up a fraction of the cold gas, expelling it from the disk. SAMs generally assume that supernova (SN) feedback can affect the interstellar medium (ISM) and hot halo gas in three distinct ways: (i) a fraction of the disk ISM can be “re-heated” from the cold phase to the hot phase, where the re-heated gas is mixed with the hot halo gas; (ii) a fraction or all of the re-heated gas can be directly ejected from the host halo without mixing with the hot halo gas; and (iii) if the SN energy from all galaxies in a halo is sufficiently large, the hot gas in the host halo can be heated, causing a fraction of the halo hot gas to be ejected from the halo itself. Gas that is ejected from the halo is stored in a separate reservoir and may be re-accreted later — we return to this below.

In all three models, the mass flux that is re-heated from the cold gas is proportional to star formation rate,

$$\dot{m}_{\text{out}} = f_{\text{ld}} SFR, \quad (16)$$

where the coefficient f_{ld} is frequently referred to as the ‘mass-loading’ factor. Different models have different loading factors and treatments for the ejection, which are described below for our three models.

In addition, all three models assume that the ejected gas can re-collapse into the halo at later times as hot halo gas. As in Springel et al. (2001) and De Lucia & Blaizot (2007), the rate of re-infall of rejected gas is given by

$$\dot{m}_{\text{re-infall}} = \chi_{\text{ri}} \left(\frac{M_{\text{ej}}}{\tau_{\text{dyn}}} \right). \quad (17)$$

Here, χ_{ri} is a free parameter, M_{ej} is the total mass of gas in the ‘ejected’ reservoir and $\tau_{\text{dyn}} = R_{\text{vir}}/V_{\text{vir}}$ is the dynamical time of the halo.

2.5.1. The Croton model

This model assumes that the amount of cold gas reheated from the disk depends only on the star formation rate, e.g.

$$\dot{m}_{\text{rh}} = \alpha_{\text{LD}} SFR, \quad (18)$$

where $\alpha_{\text{LD}} = 3.5$, consistent with observations of Martin (1999). The total amount of energy released by SN explosions and coupled into feedback over the relevant time interval during which an amount $SFR\Delta t$ of stellar mass formed is written as

$$\Delta E_{\text{SN}} = 0.5\alpha_{\text{SN}} V_{\text{SN}}^2 SFR\Delta t, \quad (19)$$

where $0.5V_{\text{SN}}^2$ is the mean energy in kinetic form injected by supernovae per unit mass of star formation, which is taken to be $V_{\text{SN}} = 630 \text{ km s}^{-1}$, and the parameter α_{SN} controls the efficiency with which this energy can actually power feedback. The amount of energy required to adiabatically reheat Δm_{rh} of cold gas and add it to the hot halo reservoir is

$$\Delta E_{\text{rh}} = 0.5\Delta m_{\text{rh}} V_{\text{vir}}^2. \quad (20)$$

If $\Delta E_{\text{excess}} = \Delta E_{\text{SN}} - \Delta E_{\text{rh}}$ is positive then enough energy is provided to physically unbind some fraction of

the hot gas from the halo. The mass of the ejected hot gas is then

$$\Delta M_{\text{ej}} = \frac{\Delta E_{\text{excess}}}{E_{\text{hot}}} M_{\text{hot}} = \left(\alpha_{\text{SN}} \frac{V_{\text{SN}}^2}{V_{\text{vir}}^2} - \alpha_{\text{LD}} \right) SFR\Delta t, \quad (21)$$

where E_{hot} represents the binding energy of the hot halo gas, $E_{\text{hot}} = 0.5M_{\text{hot}}V_{\text{vir}}^2$. This ejected gas is added to an external reservoir of material, M_{ej} . Ejected material may fall back into the potential well of the halo at a later time and be added back to the hot component, as described above. The model parameters are $\alpha_{\text{LD}} = 3.5$, $\alpha_{\text{SN}} = 0.35$, and $\chi_{\text{ri}} = 0.5$.

2.5.2. The Somerville model

The mass reheating rate of the cold gas in the Somerville model is given by

$$\dot{m}_{\text{rh}} = \alpha_{\text{LD}} \left(\frac{V_{\text{disk}}}{200 \text{ km s}^{-1}} \right)^{-\beta_{\text{LD}}} SFR, \quad (22)$$

where α_{LD} and β_{LD} are free parameters. The circular velocity of the disk, V_{disk} , is taken to be the maximum rotation velocity of the (uncontracted) dark matter halo, V_{max} . After the gas is removed from the galaxy it can either be trapped within the potential well of the dark matter halo and deposited into the hot gas reservoir, or ejected from the halo into the intergalactic medium (IGM). This model assumes that a fraction of the re-heated gas can be blown out of the halo, governed by

$$f_{\text{ej}}(V_{\text{vir}}) = \left[1 + \left(\frac{V_{\text{vir}}}{V_{\text{EJ}}} \right)^{\beta_{\text{EJ}}} \right]^{-1}, \quad (23)$$

with β_{EJ} and V_{EJ} as free parameters. This function behaves as a smoothed step function. For halos with V_{c} much higher than V_{EJ} , a negligible fraction of re-heated gas is expelled out of the halo, and for halos with V_{vir} much lower than V_{EJ} all re-heated gas leaves the halo and is deposited into M_{ej} , where it is again subject to re-infall at late times.

2.5.3. The Lu model

The Lu model assumes the loading factor for SN feedback is a power-law function of halo circular velocity, similar to the Somerville model:

$$f_{\text{ld}} = \alpha_{\text{LD}} \left(\frac{V_{\text{vir}}}{V_0} \right)^{-\beta_{\text{LD}}}, \quad (24)$$

where the power index β_{LD} and the normalization α_{LD} are model parameters, and V_0 is an arbitrary scale, which is fixed at 220 km/s. To compute the fraction of gas that is ejected from the halo, the model follows the same parameterization as the Somerville model (Eq. 23). Again, for a halo with a circular velocity lower than V_{EJ} , most of the outflow gas is ejected out of the halo, while for halos with circular velocities much larger than V_{EJ} , the ejected fraction follows a power-law function of the halo circular velocity.

In addition to reheating and ejecting the cold gas, the Lu model also expels the hot halo gas in a similar way as the Croton model. If there is still extra SN energy left after reheating and ejection, the surplus is assumed to

power a wind, and the mass of the wind can be written as

$$\Delta m_{\text{wind}} = \epsilon_W \left\{ \alpha_{\text{SN}} \frac{V_{\text{SN}}^2}{V_{\text{esc}}^2} - f_{\text{ld}} \left[\left(\frac{V_{\text{vir}}}{V_{\text{esc}}} \right)^2 + f_{\text{ej}} \right] \right\} SFR \Delta t, \quad (25)$$

where V_{esc} is the escape velocity of the halo. For a NFW halo with a concentration c (Navarro et al. 1996), $V_{\text{esc}} = V_{\text{vir}} \times \sqrt{\frac{2c}{\ln(1+c) - \frac{c}{1+c}}}$. For halos with $V_{\text{vir}} = 100 \text{ km/s}$ at $z = 0$, the concentration is typically $\gtrsim 10$ in the current Λ CDM model (e.g. Zhao et al. 2009; Prada et al. 2012), giving $V_{\text{esc}}^2 \approx 13V_{\text{vir}}^2$. In total, there are 5 parameters – α_{LD} , β_{LD} , β_{EJ} , V_{EJ} , and ϵ_W – governing SN feedback in this model. Note that when β_{LD} and β_{EJ} in the Lu model is set to be 0, and V_{esc} and V_{vir} are not distinguished, the Lu model is reduced to the Croton model. Similarly, when ϵ_W in Eq. 25 is 0, the Lu model reduces to the Somerville model.

2.6. AGN feedback and Halo quenching model

The sharp decline of the number density of galaxies at the high mass/luminosity end of the galaxy mass/luminosity function suggests a mechanism (or mechanisms) at work in high mass halos to effectively suppress star formation. The large reservoirs of hot gas that are detected observationally in massive halos further suggest that cooling is also suppressed. Recent models implementing the feedback from supermassive black holes have demonstrated that AGN activity can shut off radiative cooling of the hot halo gas and quench star formation in high-mass galaxies (Croton et al. 2006; Bower et al. 2006; Cattaneo et al. 2007; Somerville et al. 2008). Although both the Croton model and Somerville model make different assumptions about the details of the AGN feedback processes, they share a common conceptual picture of the growth of supermassive black hole mass and its feedback. In these two models, the black holes grow their mass and affect galaxy formation through two different modes: quasar mode and radio mode. The quasar mode is the bright mode of black hole growth observed as optical or X-ray bright AGN radiating at a significant fraction of their Eddington limit ($L \approx (0.1 - 1)L_{\text{Edd}}$) (Vestergaard 2004; Kollmeier et al. 2006). Such bright AGNs are believed to be fed by optically thick, geometrically thin accretion disks (Shakura & Sunyaev 1973). In these models, the quasar mode is assumed to be triggered by merger events, which also increase the mass of the galactic bulge. A large fraction of massive galaxies are detected at radio wavelengths (Best et al. 2007) without showing the characteristic emission lines of classical optical or X-ray bright quasars (Kauffmann et al. 2008). Their accretion rates are believed to be a small fraction of the Eddington rate and they are radiatively extremely inefficient. Although AGN spend most of their time in the radio mode, they gain most of their mass during the short and Eddington-limited quasar mode.

For the Croton model and the Somerville model in this paper, the quasar phase is triggered solely by galaxy merger events. Whenever the two progenitor galaxies merge, their black holes are assumed to also merge and form a single black hole whose mass is the sum of the

progenitor black holes' masses. After that, rapid gas accretion onto the black hole occurs. This is motivated by the gas inflow into the nuclear regions of galaxies seen in disk merger simulations (Springel et al. 2005; Cox et al. 2006; Hopkins et al. 2006, 2007; Robertson et al. 2006). During the merger, the black hole is assumed to grow rapidly with accretion rates near the Eddington limit. This rapid accretion continues until the energy being deposited into the ISM in the central region of the galaxy is sufficient to significantly offset and eventually halt accretion via a pressure-driven outflow. We now describe the models in more detail for both quasar and radio mode, and their effect on galaxy formation.

2.6.1. The Croton model

In the Croton model, during a quasar mode event progenitor black holes are assumed to coalesce with no loss of mass due to dissipative processes. A fraction of the cold gas of the progenitor galaxies is also accreted by the central black hole, causing the black hole mass to increase by:

$$\Delta m_{\text{BH,quasar}} = \frac{f_{\text{BH}} M_{\text{cold}} M_{\text{sat}} / M_{\text{central}}}{1 + (280 \text{ km s}^{-1} / V_{\text{vir}})^2}, \quad (26)$$

where M_{central} and M_{sat} are the cold baryon mass (stars and cold gas) of the central galaxy and the merging satellite, and f_{BH} is a free parameter governing the efficiency of the accretion event. As described above, the quasar mode is the dominant growth mechanism for black holes in the model. The version of the Croton model we adopt in this paper calculates the total energy in a quasar wind multiplied by a coupling parameter, $E_{\text{quasar}} = 0.1 \eta_{\text{AGN}} \Delta m_{\text{BH,quasar}} c^2$, and the binding energy of the cold gas in the galaxy, $1/2 M_{\text{cold}} V_{\text{vir}}^2$, and the binding energy of the hot gas in the halo, $1/2 M_{\text{hot}} V_{\text{vir}}^2$. The model then compares the energy radiated by the quasar and the binding energy of the cold gas. If the quasar energy is larger than the cold gas binding energy, all the cold gas is ejected from the disk and its mass is added into the ejected reservoir. If the quasar wind energy is larger than the combined cold and hot gas binding energy, then the model ejects both the cold and hot gas. It is worth noting that the Croton model does not explicitly impose an Eddington limit for the accretion rate in the quasar mode and, therefore, does not make assumptions about black hole seed mass.

The second mode of AGN, the radio mode, also enables the black hole to gain mass, but generally at a much slower rate. In contrast to the quasar mode, the radio mode has low Eddington ratio accretion rates, is radiatively inefficient and is associated with efficient production of radio jets and buoyant bubbles that can heat gas in a quasi-hydrostatic hot halo. Here, the accretion is from the surrounding hot gas and is assumed to be continuous as long as a hot halo is present. In the Croton model, it is characterized by the following simple relation:

$$\dot{m}_{\text{BH,radio}} = \kappa_{\text{AGN}} \left(\frac{M_{\text{BH}}}{10^8 M_{\odot}} \right) \left(\frac{f_{\text{hot}}}{0.1} \right) \left(\frac{V_{\text{vir}}}{200 \text{ km s}^{-1}} \right)^3, \quad (27)$$

where κ_{AGN} is a free parameter governing the rate of the black hole mass growth in the radio mode, and f_{hot} is the

fraction of the mass of the halo in the hot gas component. In contrast to the quasar mode, the radio mode results in the injection of feedback energy directly into the hot halo gas. The injected energy is

$$L_{\text{heat}} = \eta_{\text{AGN}} \dot{M}_{\text{BH}} c^2, \quad (28)$$

where η_{AGN} is a free parameter governing the efficiency of radio mode heating. Assuming that gas is thermalized to the virial temperature of the halo, the heating rate is

$$\dot{m}_{\text{heat}} = \frac{L_{\text{heat}}}{1/2V_{\text{vir}}^2}. \quad (29)$$

The net cooling rate is then the usual cooling rate minus the heating rate. Radio mode feedback can result in a reduction, or even complete cessation, of cooling onto the disk, depending on how this heating rate compares with the cooling rate of the halo gas. This can have a dramatic effect on the production of new stars, especially in massive galaxies.

2.6.2. The Somerville model

The Somerville model seeds a black hole with mass $\sim 100M_{\odot}$ for every top-level progenitor halo in the merger tree. When galaxy-galaxy mergers occur, and hence a quasar mode event is triggered, the final black hole mass $m_{\text{BH,final}}$ at the end of the blow-out phase is assumed to be related to the mass of the spheroidal component after the merger. The limiting black hole mass is given by the following black hole mass to spheroid mass ratio scaling relation from simulations (Hopkins et al. 2007),

$$\log\left(\frac{M_{\text{BH},0}}{M_{\text{sph}}}\right) = -3.27 + 0.36 \cdot \text{erf}[(f_{\text{cold}} - 0.4)/0.28], \quad (30)$$

with a scatter around the relationship of $\sigma_{\text{BH}} \sim 0.2 - 0.3\text{dex}$, where σ_{BH} is a free parameter. For the model adopted in this paper, $\sigma_{\text{BH}} = 0.3\text{dex}$. In the above scaling relation, f_{cold} is simply the cold gas fraction of the combined merging galaxy pair, $f_{\text{cold}} = M_{\text{cold}}/(M_{\text{cold}} + M_{*})$. The final black halo mass is the value of the black hole mass computed from Eq.30 times a free parameter, $f_{\text{BH,FINAL}}$, e.g.

$$M_{\text{BH,final}} = f_{\text{BH,FINAL}} M_{\text{BH},0}. \quad (31)$$

The value of $f_{\text{BH,FINAL}}$ is taken from numerical hydro simulations of galaxy mergers.

During the quasar phase, black holes increase their mass in two different growth regimes: an Eddington-limited phase and a power-law decline phase of accretion. In the first regime, the black hole accretes at the Eddington limit until it reaches a critical black hole mass $M_{\text{BH,crit}}$. Following the numerical simulations of Hopkins et al. (2007) and the family of light curves defined by Hopkins et al. (2006), the Somerville model assumes that

$$M_{\text{BH,crit}} = 1.07 f_{\text{BH,C}} \left(\frac{M_{\text{BH,final}}}{10^9 M_{\odot}}\right)^{1.1}, \quad (32)$$

where the coefficient $f_{\text{BH,C}}$ determines how much of the black hole growth occurs in the Eddington-limited versus the power-law decline phase. It is set to be $f_{\text{BH,C}} = 0.8$ according to the merger simulations.

The model assumes that, when $M_{\text{BH}} < M_{\text{BH,crit}}$, the black hole is in the Eddington-limited phase, where the black hole accretes mass at a fraction of the Eddington limit. When the black hole mass exceeds the critical mass $M_{\text{BH,crit}}$, the black hole enters the ‘blow-out’ phase, which is modeled by a power-law decline in the accretion rate according to the light curves found in merger simulations from Hopkins et al. (2006). This accretion drives a galactic wind. The outflow mass flux powered by this galactic wind is

$$\dot{M}_{\text{out,Q}} = \epsilon_{\text{wind}} \cdot \eta_{\text{rad}} \cdot \frac{c}{V_{\text{esc}}} \cdot \dot{M}_{\text{acc}}. \quad (33)$$

When the black hole reaches the mass $M_{\text{bh,final}}$, the accretion onto the black hole shuts off. This part of the model is detailed in Hirschmann et al. (2012). Readers are referred to this paper for a description.

For the radio mode, the Somerville model assumes a Bondi-Hoyle-type accretion combined with an isothermal cooling flow solution (Nulsen & Fabian 2000). The model calculates the accretion rate in the radio mode by

$$\dot{M}_{\text{radio}} = \kappa_{\text{radio}} \left[\frac{kT}{\Lambda(T, Z)}\right] \left(\frac{M_{\text{BH}}}{10^8 M_{\odot}}\right), \quad (34)$$

where T and Z are the temperature and metallicity of the hot halo gas, and $\Lambda(T, Z)$ is the cooling function. The central black hole accretes at this rate whenever hot halo gas is present (“hot-mode” accretion, $r_{\text{cool}} < R_{\text{vir}}$). The energy associated with this accretion effectively couples to and heats the hot gas and is given by

$$L_{\text{heat}} = \kappa_{\text{heat}} \eta_{\text{rad}} \dot{M}_{\text{BH,radio}} c^2. \quad (35)$$

The model assumes a similar heating rate to the Croton model (Eq. 29) but with a slightly different coefficient,

$$\dot{m}_{\text{heat}} = \frac{L_{\text{heat}}}{3/4V_{\text{vir}}^2}. \quad (36)$$

2.6.3. The Lu model

The Lu model does not include an explicit black hole accretion and AGN feedback model. However, it adopts a halo quenching model to mimic the effects of AGN feedback that stops radiative cooling in high mass halos (Cattaneo et al. 2006; Bower et al. 2006). In the model, when the halo mass exceeds a critical quenching mass threshold, M_{cc} , radiative cooling of the hot halo gas ceases. For each merger tree, the Lu model draws a random number for $\log M_{\text{cc}}$ from a normal distribution with a mean $\log M_{\text{CC},0}$ and a standard deviation σ_{CC} . When a halo in the merger tree has a virial mass higher than M_{cc} the radiative cooling of the halo is switched off. $\log M_{\text{CC},0}$ and σ_{CC} are taken as free parameters. We find that the rapid declining high-mass end of the stellar mass function constrains $M_{\text{CC},0}$ to be around $10^{12} M_{\odot}$, and $\sigma_{\text{CC}} \sim 0.3$ dex.

2.7. Satellite galaxies: dynamical friction and galaxy mergers

2.7.1. The Croton model

The Croton model makes use of the subhalo information from the simulation merger tree whenever the subhalo is resolved. The version of the Croton model we

adopt in this paper implements a new prescription for satellite galaxies (Croton et al. in prep). Here, subhalos are treated in a similar way to primary halos. Firstly, subhalos are allowed to host hot gas, which can cool to fuel the central galaxy of the subhalo. The radiative cooling is treated in the same way as that described in Section 2.3. Unlike the primary halos, however, subhalos cannot acquire more baryons from the hot halo of the host primary halo. When the halo mass of the subhalo decreases due to tidal stripping, the hot gas of the subhalo is stripped in proportion to the dark matter mass stripping. Note that, for simplicity, any gas that is ejected from a subhalo due to SN or quasar winds is added to the primary halo ejected component, not the subhalo. This gas can then be reincorporated at a later time into the primary halo.

The Croton model has also implemented a new prescription to determine the fate of satellite galaxies that are orbiting within larger primary halos. First, the model adopts the dynamical friction formula (Binney & Tremaine 1987) to calculate the *average* merger time for a subhalo upon infall

$$t_{\text{fric}} = \frac{1.17 r_{\text{sub}}^2 V_{\text{vir}}}{\ln \Lambda G M_{\text{sub}}}, \quad (37)$$

where $r_{\text{sub}} = R_{\text{vir}}$ and M_{sub} are the radial distance of the subhalo from the center of the host and subhalo mass of the satellite galaxy measured at infall, and $\ln \Lambda$ is the Coulomb logarithm, approximated as $\ln \Lambda = \ln(1 + M_{\text{vir}}/M_{\text{sub}})$. Second, the model keeps track of the dark matter mass of the hosting subhalo to galaxy mass (cold gas mass plus stellar mass) ratio for every subhalo. The model adopts a critical halo mass to galaxy mass ratio, $f_{\text{ST,crit}}$, as a model parameter. When the dark matter mass hosting the satellite is stripped such that the subhalo mass to galaxy mass ratio drops below this critical ratio, the model determines the fate of the subhalo galaxy according to the estimated dynamical friction timescale. If the subhalo has survived longer than the expected average dynamical friction times, this implies the subhalo is more bound than average and hence the model merges the galaxy with the central galaxy and removes the subhalo from the tree. If the subhalo reaches the critical mass ratio before the dynamical friction time, this implies the subhalo was less bound than average, and the model completely strips the galaxy and adds its stellar mass into the diffuse stellar mass component of the primary halo, with any remaining satellite gas going into the primary hot component. Thus, in the Croton model there are no orphan galaxies (satellite galaxies without host subhalos), because when a subhalo is significantly stripped, the hosted galaxy is either merged into the central galaxy or completely disrupted.

For satellites that do merge, the treatment of the merger remnant depends on the mass ratio of the two galaxies, $M_{\text{sat}}/M_{\text{central}}$, where M_{sat} and M_{central} are the cold baryon masses, stellar mass plus cold gas mass, of the satellite and the central galaxy. Mergers are considered major or minor depending on whether $M_{\text{sat}}/M_{\text{central}}$ is larger or smaller than the value of the free parameter, f_{MG} . The Croton model adopts $f_{\text{MG}} = 0.3$.

For a minor merger, the satellite's stars are added to

the central bulge, and its gas is added to the central disk. For a major merger, the model combines all the existing stars from the two merging galaxies into a central galaxy, which is now assumed to be spheroidal. All mergers trigger a star-burst, and all stars formed in the burst are added into the central spheroidal component of the galaxy. A fraction, e_{burst} , of the combined cold gas in the two merging progenitors becomes stars, and the rest of the gas joins the gaseous disk. The Croton model assumes that e_{burst} depends on the ratio of the baryon masses of the two galaxies:

$$e_{\text{burst}} = \alpha_{\text{burst}} (M_{\text{sat}}/M_{\text{central}})^{\beta_{\text{burst}}}, \quad (38)$$

as in the so-called ‘collisional star-burst model’ of Somerville et al. (2001).

2.7.2. The Somerville model

In the Somerville model, when a lower mass halo merges into a higher mass halo, the hot gas associated with the lower mass one is instantaneously stripped and added into the hot gas of the primary halo. In the subsequent evolution, the Somerville model does not use the subhalo information from the N -body simulation to follow the satellite galaxies. Instead, it adopts a version of the dynamical friction model proposed by Boylan-Kolchin et al. (2008) right after a galaxy enters the virial radius of a larger halo. The dynamical friction timescale is modeled

$$t_{\text{fric}} = A \frac{(M_{\text{vir},1}/M_{\text{vir},2})^b}{\ln(1 + M_{\text{vir},1}/M_{\text{vir},2})} \exp(c\eta) \left[\frac{r_c(E)}{R_{\text{vir}}} \right]^d \tau_{\text{dyn}}, \quad (39)$$

where $M_{\text{vir},1}$ and $M_{\text{vir},2}$ are the virial mass of the primary and secondary halos before merging, $\eta = j/j_c(E)$ is the specific angular momentum relative to a circular orbit with the same energy, $r_c(E)$ is the circular radius of a circular orbit with the same orbital energy, and τ_{dyn} is the dynamical time scale of the primary halo, $\tau_{\text{dyn}} = R_{\text{vir}}/V_c$. The parameters defined in the formula are fixed to the values derived by Boylan-Kolchin et al. (2008) based on numerical simulations, $A = 0.216$, $b = 1.3$, $c = 1.9$, $d = 1.0$.

When it first becomes a satellite, each sub-halo is assigned a value of η and $r_c(E)$ by choosing η in the interval $0 \leq \eta \leq 1$ from a Gaussian distribution with mean 0.5 and dispersion $\sigma = 0.214$, and choosing $r_c(E)/r_{\text{vir}}$ from a uniform distribution on the interval $[0.6 - 1]$. Zentner et al. (2005) showed that this is a good representation of the satellite orbits in cosmological simulations.

Following Taylor & Babul (2001), the model accounts for tidal stripping as the satellite orbits within the host halo. The rate of mass loss due to tidal stripping is calculated via:

$$\zeta = -\log[f_{\text{strip}}(0.35\eta^2 - 0.2\eta + 0.58)] \quad (40)$$

where f_{strip} is an adjustable parameter. The satellite mass at each time-step is then given by:

$$m_{\text{strip}} = m_i \exp(-\zeta t_{\text{acc}}/P) \quad (41)$$

where m_i is the mass of the satellite at infall, t_{acc} is the time since infall, and $P = 2\pi\tau_{\text{dyn}}$ is the orbital period. When the mass of satellite falls below a fraction, f_{dis} , of the mass enclosed by r_s , the Navarro-Frenk-White scale

radius, the satellite is considered ‘disrupted’. The parameter, f_{dis} , is here set equal to unity. The cold gas within a disrupted satellite is added to the hot gas reservoir of the host halo, the stars are added to a ‘diffuse’ stellar halo, and the halo is removed from all further calculations. The treatment of subhalo merging and disruption has been tested by comparing with the results from high resolution dissipationless cosmological N-body simulations. The model reproduces the subhalo conditional mass function and radial distribution of surviving subhalos.

In the Somerville model, a more sophisticated starburst model is adopted. At the beginning of a galaxy merger, the model allocates a reservoir of ‘burst fuel’ $m_{\text{burst}} = e_{\text{burst}} M_{\text{cold}}$, where M_{cold} is the combined cold gas from both of the progenitor galaxies. The burst continuously converts a fraction of this fuel into stars until it is exhausted. The efficiency parameter e_{burst} and the timescale τ_{burst} for the burst-mode star formation depend on the baryonic mass ratio of the two progenitors, the combined cold gas content of the merging galaxies, the bulge-to-total stellar mass ratio, virial velocity of the host halo and redshift of the merger. The recipe for the starburst efficiency and timescale functions of these variables is based on hydrodynamic simulations of binary galaxy mergers (Robertson et al. 2006; Cox et al. 2008). We refer to Somerville et al. (2008) (Section 2.5.2 and reference therein) for details of the model. In the models used here, we use the updated model for the burst efficiency presented in Hopkins et al. (2009).

2.7.3. The Lu model

Like the Croton model, the Lu model uses the subhalo information in the merger trees to follow the satellite population. Unlike the Croton model, however, the model estimates the dynamical friction timescale from the time when the subhalo is no longer resolved in the simulation. When the identification of a subhalo disappears in the merger tree, the model keeps the satellite galaxy hosted by the subhalo orbiting in the main halo for a dynamical friction time, t_{fric} , defined above by Equation 37 (Binney & Tremaine 1987). To calculate this time the properties of the satellite and the host halo at the time when the subhalo was last identified are used (this differs from the Croton model where t_{fric} is calculated upon initial infall of the subhalo). If the main halo merges into another halo before this merger time is reached, a new value for the merger time is calculated and the merger clock is restarted.

The Lu model assumes that satellite galaxies will merge into the central galaxy of the host halo after a time t_{orb} since the satellite’s host subhalo is no longer resolved in the simulation. To allow uncertainty for the estimation of the dynamical friction time scale, the model adopts a factor f_{DF} of t_{fric} to be the orbiting time scale, i.e.

$$t_{\text{orb}} = f_{\text{DF}} t_{\text{fric}} \quad (42)$$

where f_{DF} is a free parameter. When two galaxies merge, the Lu model also assumes that a certain amount of cold gas from the two merging galaxies is converted into stars in a starburst. To do this, the Lu model follows the same model assumed by Eq. 38, with α_{burst} and β_{burst} as free parameters.

2.8. Chemical enrichment

All three models assume that when a parcel of new stars form, dM_* , a certain mass of metals, $dM_Z = y dM_*$, is created and instantaneously mixed back into the cold gas in the disk. A Chabrier (2003) initial mass function (IMF) and a constant yield of $y = 1.5 Z_{\odot}$ is taken throughout.

New stars have the average metallicity of the cold gas at the time they formed. When cold gas is blown out of the disk due to SN or quasar winds, the associated metals are mixed with either the hot gas or ejected from the halo altogether in the same proportion as they were re-heated. Note that all the three models adopt the instantaneous recycling assumption, meaning that some fraction of the mass that is turned into stars at each time-step is instantaneously returned to the cold gas disk due to very short lived stars and mass lost from stellar winds. For a Chabrier IMF the recycling fraction is $f_{\text{rec}} = 0.43$. We also deposit the new metals into the cold gas.

2.9. Semi-empirical model

In this paper we also compare some of the SAM predictions with the semi-empirical model of Behroozi et al. (2013b), which is built on the same halo merger trees. The semi-empirical results are derived in a very different way than the traditional semi-analytic models discussed above. Rather than parameterizing the physics of star formation, Behroozi et al. (2013b) use a flexible parametrization for the stellar mass–halo mass relationship, $SM(M_h, z)$. This comprises six parameters to control the relationship at fixed redshift, including a characteristic stellar mass, halo mass, faint-end slope, massive-end cutoff, transition region shape, and scatter. For each parameter set, three secondary parameters control the redshift scaling at low ($z = 0$), mid ($z \sim 1$) and high ($z > 3$) redshift. Additional nuisance parameters account for systematic uncertainties in converting between galaxy luminosities and stellar masses/star formation rates.

A specific choice of $SM(M_h, z)$ applied to the halo merger trees will result in predictions for observed stellar mass functions, cosmic star formation rates, and specific star formation rates. Comparing these predictions to observed data from $z = 0$ to $z \sim 8$ results in a likelihood for a given choice of $SM(M_h, z)$. The posterior distribution for $SM(M_h, z)$, along with derived values for the average star formation rate as a function of halo mass and redshift, are then inferred from observed data using an MCMC approach. The full details of this method are presented in Behroozi et al. (2013b).

3. METHODOLOGY

3.1. Merger trees

The merger trees employed for the SAMs in this paper are extracted from the Bolshoi N-body cosmological simulation (Klypin et al. 2011). It was run in a volume $250 h^{-1} \text{Mpc}$ on a side using ~ 8 billion particles with mass and force resolution adequate to follow subhalos down to the completeness limit of $V_{\text{max}} = 50 \text{km s}^{-1}$ (halo maximum circular velocity). There are 180 stored time steps for merger tree construction, which should yield stable SAM predictions for low- z galaxy properties (Benson 2012). Dark matter halo finding was

done with the Rockstar code (Behroozi et al. 2013c). The approach is based on adaptive hierarchical refinement of friends-of-friends groups in six phase-space dimensions and one time dimension, which allows for robust (grid-independent, shape-independent, and noise-resilient) tracking of substructure. The merger trees were generated using the Consistent Trees algorithm, which simulates the gravitational motion of halos, to improve the completeness and purity of both merger trees and halo catalogs (Behroozi et al. 2013d).

3.2. Model Tuning

All models are tuned independently to the same calibration data set, either by “hand” or by “machinery”. We choose the stellar mass function of local galaxies estimated by Moustakas et al. (2013) as our primary calibration data set. The mass function is derived from a sample of 504,437 galaxies selected from the SDSS Data Release 7 (DR7; Adelman-McCarthy et al. 2008). The stellar mass measurements are determined from SED fitting of multiple photometric bands, including SDSS optical bands, GALEX UV bands, and 2MASS JHK_s bands and the photometry at $3.4\mu\text{m}$ and $4.6\mu\text{m}$ from the WISE All-Sky Data Release. The authors adopted the Chabrier (2003) IMF from $0.1\text{--}100 M_\odot$, as adopted in the SAMs presented here. They assumed exponentially declining star formation histories with stochastic bursts and allowed a wide range of galaxy ages and histories, adopting reasonable priors on stellar metallicity and dust attenuation. The error bars in the data include both the uncertainty due to sample size (i.e., Poisson error) and sample variance. The authors also empirically determined the stellar mass completeness limits of their sample. Galaxies with stellar mass larger than $10^9 M_\odot$ are above the surface brightness and stellar mass-to-light ratio completeness limits (Blanton et al. 2005; Baldry et al. 2008). The main constraint of the mass function for the models is from bins with $M_* \geq 10^9 M_\odot$. For further details, readers should refer to Moustakas et al. (2013).

The Lu model has been calibrated with a MCMC engine, which supports efficient model parameter space exploration. To do this, the method first defines a likelihood function, which quantifies the closeness between the model and calibration data. As the low-mass end of the stellar mass function potentially involves considerable incompleteness, they also treat this incompleteness in the likelihood model. The Lu model defines the completeness fraction as the ratio between the observed number density and the underlying number density of galaxies. For a given stellar mass bin i , the completeness fraction is $p_i = \frac{\phi_{\text{obs},i}}{\phi_i}$. If a model predicts ϕ_i for a mass bin, the expected number density of galaxies to be observed is $p_i \phi_i$. The completeness fraction p_i is assumed to be a power-law function of stellar mass as implied by the estimate of Baldry et al. (2008) who showed that the slope of the galaxy stellar mass function for mass lower than $10^{8.6} M_\odot$ can be as steep as -1.8 (solid gray line in Figure 1). Following this estimate, the Lu model assumes that p_i remains unity for $M_* > 10^9 M_\odot$ but decreases toward the low-mass end following a power law of stellar mass as

$$p_i = \left(\frac{M_{*,i}}{10^9 M_\odot} \right)^{\alpha_{\text{IN}}}, \quad (43)$$

where α_{IN} is the difference of the faint-end slope between the incomplete and the complete sample. The model adopts α_{IN} as a free parameter to allow it to change with a uniform prior between 0 and $1.80 - 1.05 = 0.75$. With this approach, if the SAM predicts a faint-end slope of -1.8 , we would expect the observed faint-end slope to be between -1.8 and -1.05 .

Taking into account the incompleteness, the χ^2 -like logarithmic likelihood for the stellar mass function is

$$\ln L = \sum_{i=0}^k \frac{(\phi_{i,\text{obs}} - p_i \phi_{i,\text{mod}}(\theta))^2}{\sigma_i^2}, \quad (44)$$

where $\phi_{i,\text{obs}}$ denotes the data points from Moustakas et al. (2013), and $\phi_{i,\text{mod}}$ denotes the model prediction from the SAM. Thus, the likelihood is not only a function of the model parameter vector θ but also a function of α_{IN} . α_{IN} is treated as a nuisance parameter and its distribution is sampled along with other parameters using MCMC. Finally, the distribution of α_{IN} is marginalized over when deriving the posterior of other model parameters (Lu et al. 2012).

For the Lu results, the MCMC is run for 6,000 iterations with 256 parallel chains using the differential evolution algorithm (Braak 2006) until converged. The convergence test is done with the Gelman-Rubin test (Gelman & Rubin 1992). We obtain 750,000 posterior samples from the MCMC to make predictions for the Lu model. For this particular run, the “best fit” model (maximum likelihood) is close to the median model of the full posterior. For the Croton model and the Somerville model, the choices of parameters are kept close to those in the published papers, but some hand-tuning has been done to get as close a fit as possible to the Moustakas et al. (2013) mass function. The exact parameter values are listed in Table 1. For the Lu model, except for a few fixed parameters, the 95% posterior range for each of free parameters is given in the parentheses in the table.

4. MODEL RESULTS

4.1. Stellar mass functions at $z = 0 - 6$

The stellar mass function of galaxies describes one of the most basic statistical properties of the galaxy population. We use the local galaxy stellar mass function (Moustakas et al. 2013) to calibrate each of the models, and then make predictions at higher redshifts. There are always uncertainties when estimating stellar masses from observational data. These uncertainties can significantly bias the stellar mass function at the high-mass end by pushing low-mass galaxies into high mass bins, thus elevating the number density estimates for the high-mass bins. In our predictions we mimic this bias by applying the simple prescription given by Behroozi et al. (2013b), who assume that the error on each model galaxy stellar mass is log normal, with a redshift dependent standard deviation, $\sigma(z) = \sigma_0 + \sigma_z z$, for the logarithmic stellar mass, where $\sigma_0 = 0.07$ and $\sigma_z = 0.04$. We convolve this error with the predicted stellar mass when computing the mass functions to compare with the observed functions at each redshift (see Behroozi et al. 2013b, for further discussion). In Figure 1, we show the stellar mass functions produced by each model at several redshifts

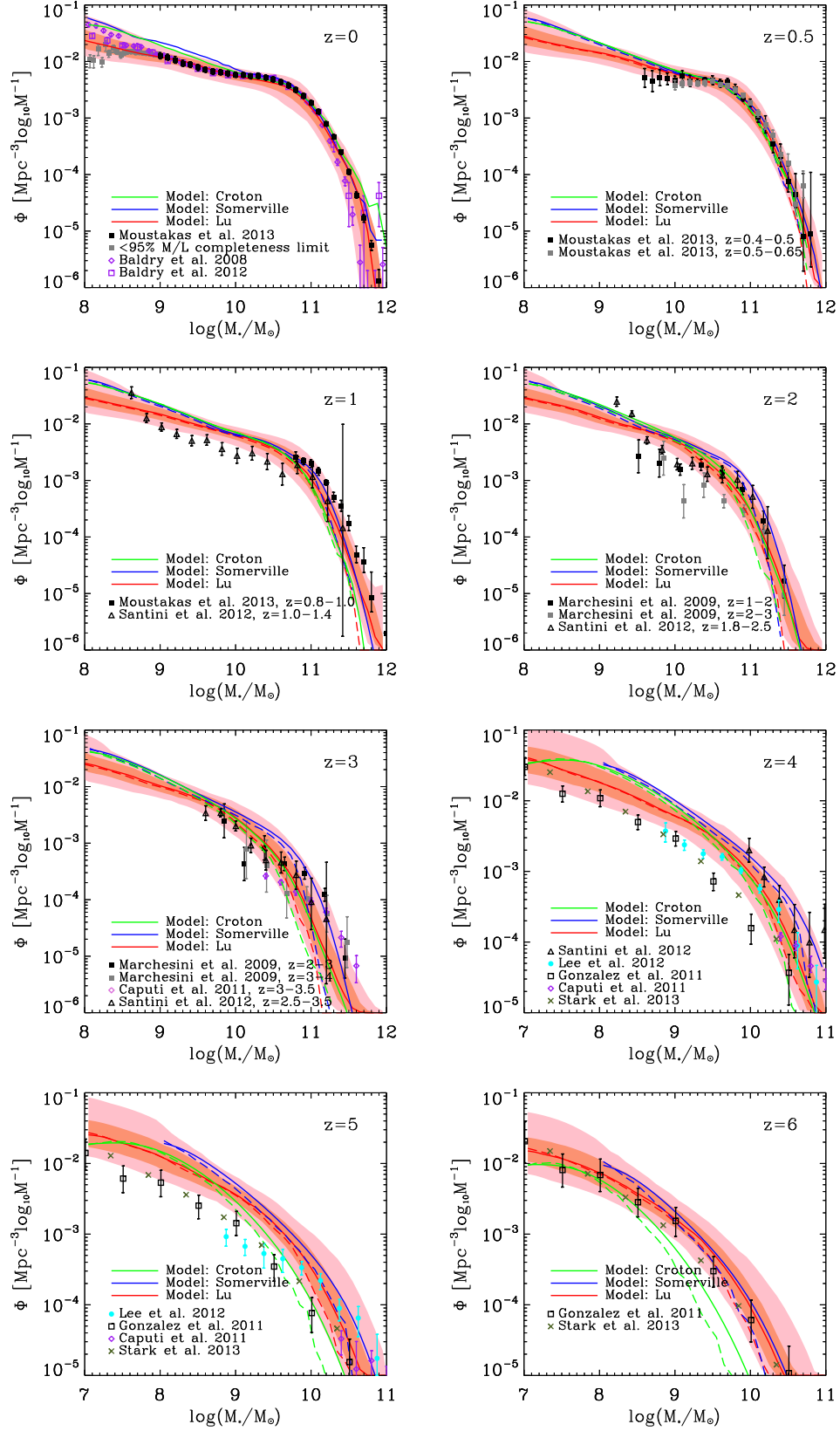


FIG. 1.— Galaxy stellar mass functions at $z = 0, 0.5, 1, 2, 3, 4, 5,$ and 6 predicted by the Croton model (green), the Somerville model (blue) and the Lu model, for which the dark and light red bands enclose 67% and 95% posterior probabilities, and the red solid line denotes the median prediction. The solid lines show the model predictions with stellar mass uncertainties convolved, and the dashed lines show the raw model predictions with no uncertainties convolved. The observational estimates for $z = 0$ are from Moustakas et al. (2013), Baldry et al. (2008), and Baldry et al. (2012). For $z = 0.5 - 6$, the data are from Moustakas et al. (2013); Marchesini et al. (2009); Santini et al. (2012); Caputi et al. (2011); Lee et al. (2012); González et al. (2011) and Stark et al. (2013) for each relevant redshift as noted in each panel. Note that only the $z = 0$ stellar mass function (Moustakas et al. 2013) is used to calibrate the models.

between $z = 0$ and 6. Each panel shows both the convolved and unconvolved versions of the predicted stellar mass functions for the three models (Croton, Somerville, and Lu).

For the Lu model, which uses MCMC to explore the model parameter space and to sample the posterior distribution of model parameters, we marginalize over the posterior probability distribution and plot the predictive distributions that enclose 67% and 95% posterior probabilities of the predicted mass function, as well as the median model posterior predictive distribution.

The first panel (upper left) shows the stellar mass function at $z = 0$, which is used to tune the models. In the panel, the black square points with error bars are the observational data from Moustakas et al. (2013). The gray squares show the stellar mass range that is below the 95% completeness limit (J. Moustakas, private communication). We also overplot the mass functions of Baldry et al. (2008) and Baldry et al. (2012), which show steeper slopes of the mass function at the low-mass end. The posterior predictive distribution from the Lu model shows that the MCMC can find models that match the constraining data remarkably well across the entire mass range. This is likewise true for the hand-tuned Croton model and the Somerville models, at least for $\log M_*/M_\odot \geq 10$. At lower stellar masses these two models overpredict the mass function by up to a factor of two. Even after doing many iterations of hand tuning, we find that it is difficult to perfectly match the low-mass end in the parameter ranges. On the other hand, the Lu model, aided by the MCMC calibration, is able to produce a low-mass-end slope as shallow as the data. We note, however, that the best models found in the Croton model and the Somerville model are generally encompassed by the 95% posterior predictive distribution of the Lu model.

Before continuing to higher redshifts, it is interesting to understand some of the key differences between the different models. The most obvious difference between the Lu model and the other two is the outflow mass-loading factor. For the Croton model, the mass-loading is assumed to be a constant at 3.5 times the SFR for all galaxies. For the Somerville model, the mass-loading factor scales with the halo maximum velocity as $\sim V_{\text{max}}^{-2.25}$. The mass-loading factor changes from 1.5 for halos with $V_{\text{max}} = 200 \text{ km s}^{-1}$ to 7.1 for halos with $V_{\text{max}} = 100 \text{ km s}^{-1}$. In the Lu model, the MCMC prefers a (perhaps extreme) model where the mass-loading factor increases with decreasing halo circular velocity by $\sim V_{\text{vir}}^{-6}$, and star formation is more strongly suppressed. For a halo with a circular velocity $V_c = 100 \text{ km s}^{-1}$, a typical mass-loading factor in the posterior of the Lu model is about 17.

The remaining panels in Figure 1 show the predicted stellar mass functions at seven other redshifts, along with accompanying observed data from each redshift range (as labeled). These observations are not used to tune any model; we simply take each $z = 0$ calibrated model and plot their higher redshift mass functions. It is encouraging that all model predictions are fairly consistent with data in all panels, out to $z \sim 6$, especially when the uncertainty in the stellar mass estimation is taken into account. As the redshift increases, the three models gradually diverge from each other, and the pos-

terior predictive distributions of the Lu model also become broader. However, because of this broadening, the diverging predictions of the two hand-tuned models remain within the 95% posterior range, with the exception of the Croton model, which predicts a relatively lower stellar mass function for $M_* > 10^9 M_\odot$ at $z \geq 5$.

In general, the divergence of the three models illustrates how different choices for the parameterization of the physical processes, and their accompanying parameter values, can lead to clear differences in higher redshift predictions. These choices are degenerate for the low-redshift stellar mass functions solely because the models are tuned against such data. This highlights the importance of obtaining accurate high- z galaxy statistics, especially for galaxy properties that can separate out the different assumptions built into SAMs through their earlier epoch consequences. In particular, the current best data sets are inconsistent with each other at the highest redshifts, making it hard to know what the “correct” answer is. For example, the model predictions for $z = 4$ are between the observational data of González et al. (2011) and Santini et al. (2012), and are fairly consistent with the data of Lee et al. (2012) and Caputi et al. (2011). The overprediction of the mass function at $z = 4 \sim 5$ compared to González et al. (2011) is possibly because the stellar mass functions of González et al. (2011) at these redshifts are derived from UV selected galaxy samples, which may potentially miss non-star-forming or dusty galaxies. Moreover, there is evidence that the nebular emission is likely to contaminate the rest-optical broadband light for galaxies at $z \sim 6-7$ (Stark et al. 2013). It has been shown that the treatment of nebular lines and assumed star formation histories can affect the stellar masses estimated from SED fitting (e.g. Schaerer et al. 2013). Data from the full CANDELS survey, analyzed in a self-consistent way, will tighten the constraints of the stellar mass functions at these redshift ranges.

In Figure 2 we integrate the stellar masses of galaxies larger than $10^8 M_\odot$ at each redshift to show the cosmic stellar mass density evolution. The three models produce similar trends and the two individual models of the Croton model and the Somerville model stay within the 95% posterior range of the Lu model. Because all the models are carefully tuned to match the stellar mass function at $z = 0$, the predicted cosmic stellar mass densities at $z = 0$ agree with each other within 10% and are consistent with the ensemble of observational data (as marked). Since the Croton model displays a more rapid evolution of the high-mass end of the stellar mass function than the Somerville model and the median of the Lu model, it predicts lower cosmic stellar mass densities at high redshifts for $z > 4$. Similarly, the Somerville model has a larger number of high-mass galaxies at higher redshifts than the Lu model, and so predicts higher cosmic stellar mass densities at those redshifts.

It is worth pointing out that although the three models make diverging predictions for the evolution of the stellar mass function at high redshift, their predicted cosmic stellar mass density as a function of redshift is in broad agreement with the data, given the large scatter between different observational estimates and their large error bars. It is obvious that the galaxy stellar mass function and its evolution is more constraining than the

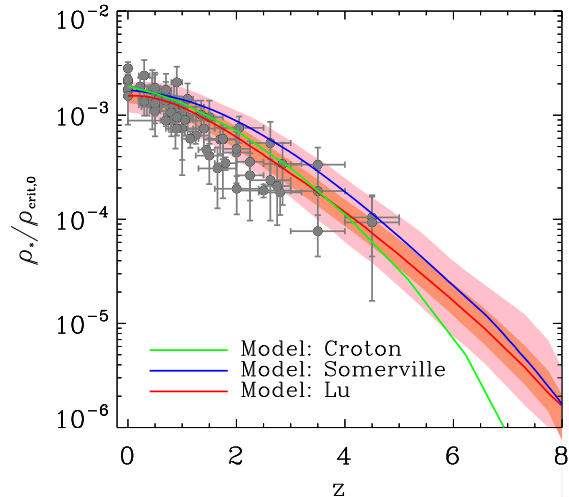


FIG. 2.— The volume averaged stellar mass density of the universe, normalized by the critical density of the universe at the present time, as a function of redshift. The filled bands denote the direct SAM predictions of 67% (dark red) and 95% (light red) posterior regions from the Lu model. The blue and green lines are predicted by the Somerville model and the Croton model. The points with error bars are various observational estimates, taken from the compilation of Wilkins et al. (2008).

evolution of the global stellar mass density.

4.2. Star formation rates

In Figure 3 we show the specific star formation rate (sSFR) vs. stellar mass for our three galaxy models (as marked), focusing on redshifts of 0, 1 and 3. The sSFR is defined as the star formation rate averaged over a time interval ~ 100 Myr normalized by the stellar mass of the galaxy. It is clear that all the models predict a clear star forming sequence, which appears to be a nearly horizontal ridge. We overplot the sSFR as a function of stellar mass of the star forming sequence of local galaxies in Salim et al. (2007) in each $z = 0$ panel of Figure 3. In observations, the star forming sequence has a width of about 0.35 dex in sSFR at $z < 1.1$ (Noeske et al. 2007), which is similar to the model predictions. However, we find that both the normalization and the slope of the star forming sequence predicted by the models differ from the observational results in detail. The overall sSFRs of the star forming galaxies in the model are systematically lower, especially for low mass galaxies. Moreover, the slope of the star forming sequence predicted by the models is shallower than the observations, especially for the Somerville model and the Lu model.

To characterize the star forming sequence predicted in the models, we find the peak sSFR on the star forming sequence for galaxies with stellar mass between $10^8 M_\odot$ and $10^{10} M_\odot$ in each model. We then draw a line at a sSFR 0.35 dex lower than the peak sSFR. We show it by a dashed magenta line in each panel of Figure 3. All models predict a star forming sequence that bends downward to lower sSFRs at high stellar masses, and an increasing number of galaxies below the magenta line when $M_* > 10^{11} M_\odot$. The trend holds at higher redshifts up to $z = 3$ as we show in the figure.

We also define another characteristic sSFR as a func-

tion of redshift defined as

$$sSFR = \frac{1}{\tau_H(z)(1 - f_{\text{rec}})}, \quad (45)$$

where $t_H(z)$ is the age of the universe at the redshift z , and $f_{\text{rec}} = 0.43$ is the assumed recycling fraction of star formation for the adopted Chabrier IMF. If a galaxy has a sSFR lower than this characteristic sSFR, it means that the time for the galaxy to accumulate its stellar mass by keeping its current star formation rate is longer than the age of the universe, suggesting that the galaxy must have had a higher star formation rate in the past to form the bulk of its stellar mass, and its SFR must have decreased. On the other hand, if a galaxy has a sSFR higher than the sSFR defined by Eq. 45, it means that the galaxy can form its stellar mass in a timescale shorter than the age of the universe with its current star formation rate, suggesting its SFR has recently increased. We also overplot this characteristic sSFR in Figure 3. We find that this characteristic sSFR closely follows the star forming sequence in each model. There is a tendency that, at high redshifts ($z > 1$), the SAM predicted star forming sequence evolves faster and becomes higher than the characteristic sSFR defined by Eq. 45 at higher redshifts. This indicates that galaxies in the models typically have a rising star formation history at high- z . We also note that the evolution of the normalization of the star forming sequence is consistent with the observational data of Noeske et al. (2007) and similar to the redshift dependence of the specific halo mass accretion rate predicted in cosmological simulations (Dekel et al. 2009). This suggests that the star formation rate of star forming galaxies at a given stellar mass follows the halo accretion rate. This is similar to what is found in empirical models (Behroozi et al. 2013b,a; Yang et al. 2013; Mutch et al. 2013b), which also match the evolution of the stellar mass function across a large redshift range.

In observations, galaxies are split into a star forming population and a quiescent population according to the sSFR for a given stellar mass (e.g. Noeske et al. 2007; Salim et al. 2007; Moustakas et al. 2013). Moustakas et al. (2013) found that their galaxy sample at $z \sim 0$ to 1 can be divided into two separate populations according to a division line defined as

$$\log\left(\frac{SFR}{M_\odot \text{yr}^{-1}}\right) = -0.49 + 0.65 \log\left(\frac{M_*}{10^{10} M_\odot}\right) + 1.07(z - 0.1). \quad (46)$$

We overplot these lines in Figure 3 for $z = 0$ and $z = 1$ and find that because the model predicted star forming sequence has a shallower slope than the dividing line, the dividing line cuts through the star forming sequence predicted by all the models at $\sim 10^9 M_\odot$. In addition, this dividing line evolves more rapidly to higher sSFRs with redshift than the models predict. For example, at $z \geq 1$ the dividing line is above the star forming sequence over a large range of stellar masses.

On the top of each sSFR- M_* diagram, we plot the fraction of galaxies that have a sSFR lower than each of the characteristic sSFR lines as a function of stellar mass. In general, all models predict a trend that the fraction of galaxies below the sSFR dividing line increases with increasing stellar masses. The fractions defined by the

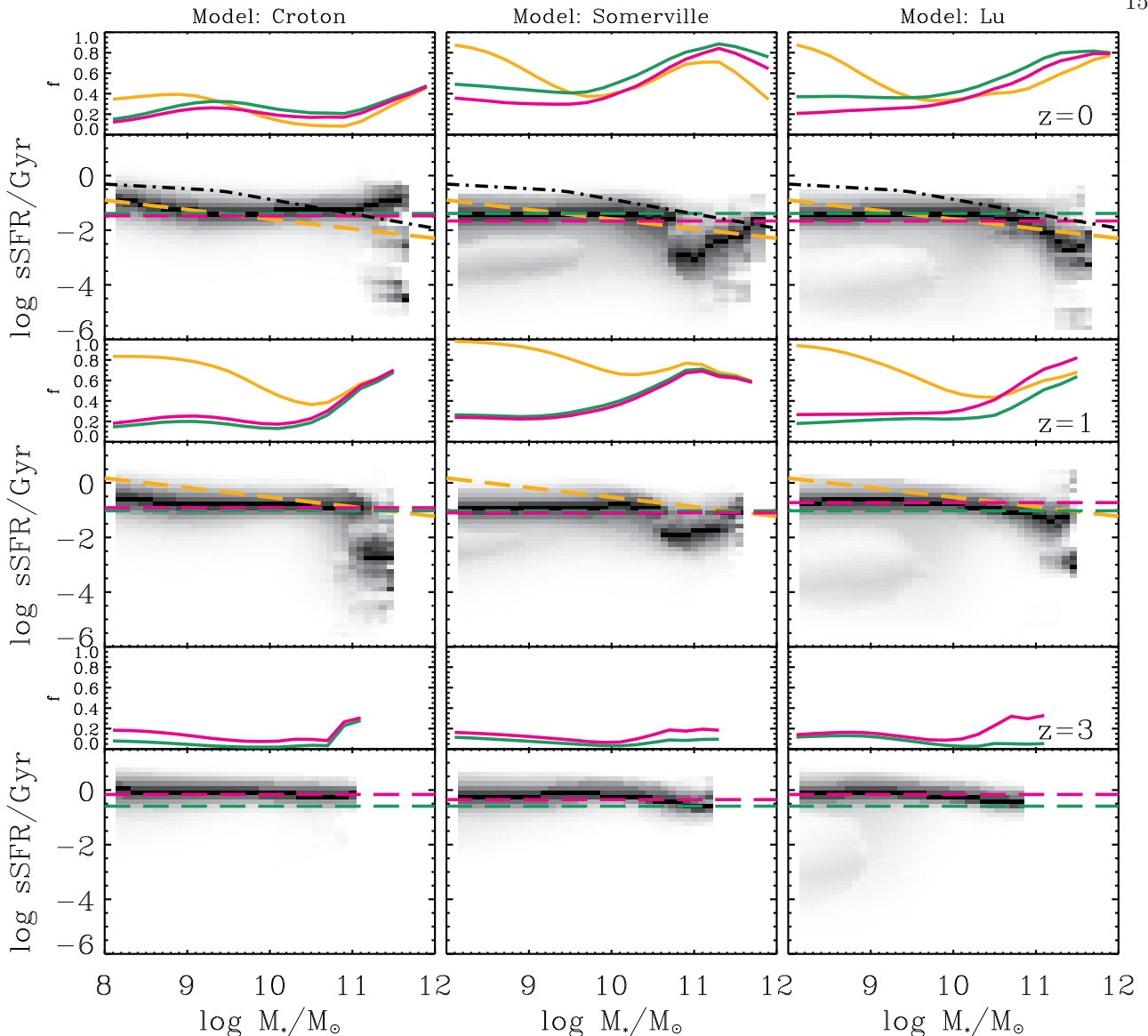


FIG. 3.— The joint distribution of specific star formation rate and stellar mass of model galaxies at $z = 0, 1$, and 3 . The first column shows the predictions of the Croton model, the second column the Somerville model, and the third column the Lu model. The black dash-dot line in the $z = 0$ panels denotes the star forming sequence from the observational study of Salim et al. (2007) for local galaxies. The orange dashed lines in the $z = 0$ and $z = 1$ panels denote the division line separating “star forming” galaxies and “quiescent” galaxies adopted in Moustakas et al. (2013). The magenta dashed lines denote the division lines that mark the sSFR 0.35 dex lower than star forming sequence produced by each model at the corresponding redshift. The green dashed lines denote the characteristic sSFR defined by Eq. 45 corresponding to the age of the universe at each redshift. On the top of each panel, we show the fraction of galaxies that have a sSFR lower than each division line as a function of galaxy stellar mass. The color coding of the lines is the same as that of the division lines in the sSFR- M_* diagram.

two dividing lines are similar for all the models. In all the models, the fraction is lower than 50% for low-mass galaxies, and the fraction goes up to nearly 90% for high-mass galaxies. The Croton model produces a relatively weaker trend at $z = 0$, but similar trend at higher redshifts. At the very highest stellar masses, the prediction of the Somerville model starts to turn over, which reflects the increasing sSFR at the very high-mass end predicted by the model. At higher redshifts, the models predict fewer galaxies below the division lines, making the predicted fractions increasingly lower. At $z = 3$, all the models predict that nearly all low-mass galaxies ($M_* < 10^{10} M_\odot$) have a sSFR higher than the characteristic sSFRs. The fraction keeps the increasing trend

at high redshifts, indicating that high-mass galaxies are getting quenched at an early cosmic epoch.

We also show the fraction based on the dividing line defined by Eq. 46, adopted in observations (Salim et al. 2007; Moustakas et al. 2013). Moustakas et al. (2013) found that in the observations the number density of galaxies is increasingly dominated by galaxies with relatively lower sSFR as stellar mass increases. In their data, for galaxies with mass $> 10^{11} M_\odot$, more than 70% are classified as “quiescent” galaxies, while for low mass galaxies, $M_* < 10^9 M_\odot$, fewer than 30% are “quiescent”. We find, however, if we adopt this dividing line, the fraction of galaxies that are below the dividing sSFR follows a different trend. Although the models reproduce the

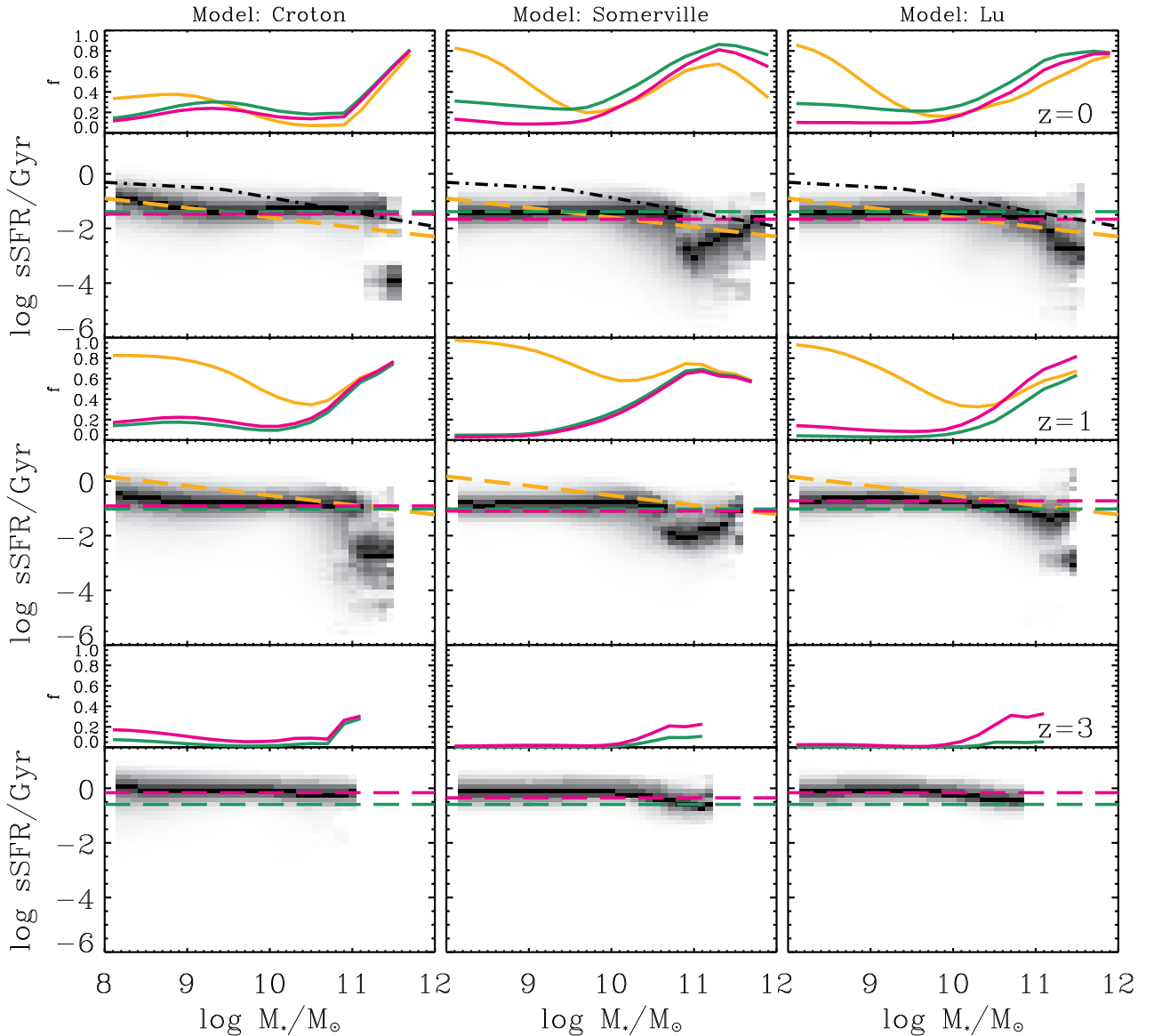


FIG. 4.— Same as Figure 3, but for central galaxies only.

trend of the data at intermediate and higher masses, they exhibit an increasing fraction as a function of decreasing stellar mass at lower stellar masses. In all models, the number of galaxies below the dividing line increases for decreasing stellar mass at the low mass end ($< 10^{9.5} M_{\odot}$) at both $z = 0$ and $z = 1$. As we discussed, the increasing trend at the low-mass end is because the star forming sequence predicted by the models is much flatter than that in observations. The dividing line adopted in observations cuts through the model star forming sequence at the low-mass end. Therefore, although the models predict a clear star forming sequence, the low-mass star forming galaxies in the models are still classified as “quiescent” galaxies by the definition of Eq. 46. These results provide a cautionary note that the “quiescent” fraction sensitively depends on the definition of “quiescent” galaxy. The comparison also demonstrates that the evolution and the mass dependence of the quiescent fraction (see, e.g. Brammer et al. 2011; Mutch et al. 2013a) provides strong constraints on models, and we plan to

investigate this in future work.

To understand how central galaxies and satellite galaxies evolve differently in the models, we show the sSFR- M_* diagram for central galaxies only in Figure 4, and satellite galaxies only in Figure 5. In fact, the star forming sequence in all models is mainly populated by central galaxies. For the highest stellar mass bins, $M_* > 10^{11} M_{\odot}$, a fraction of central galaxies appear below the dividing line for $z \leq 1$, indicating that star formation has been truncated in these galaxies. While the Somerville model predicts that the sSFR distribution of high mass galaxies is shifted about one order of magnitude lower, the peak sSFR starts to increase again for higher stellar masses. Among the three models, the Croton model predicts the largest separation in sSFR between massive quiescent galaxies and star forming galaxies. At higher redshifts, no model predicts a significant population of high-mass quiescent galaxies; almost all central galaxies at such early times are star forming.

Interestingly, the distributions of satellite galaxies in

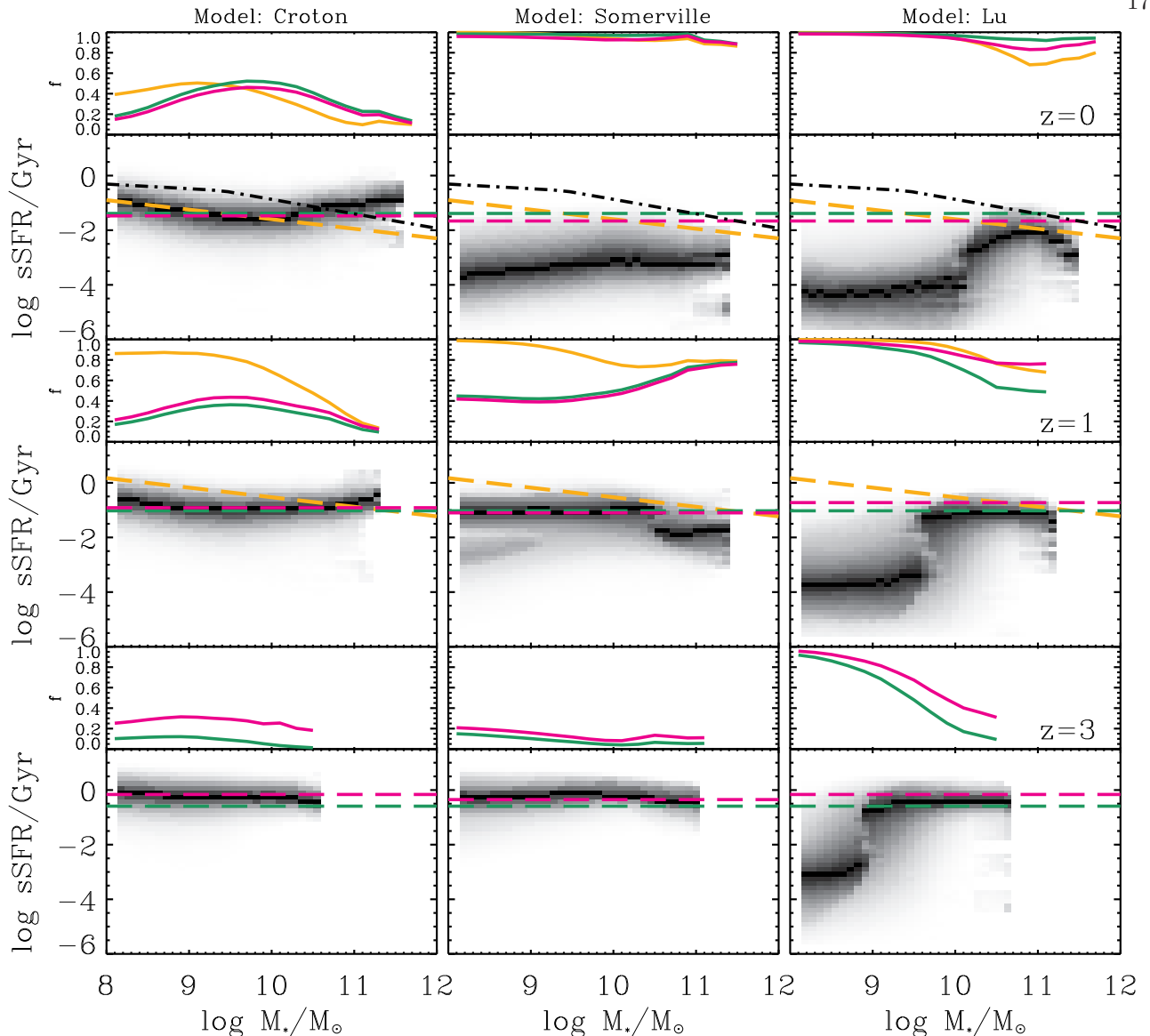


FIG. 5.— Same as Figure 3, but for satellite galaxies only.

the sSFR- M_* diagram predicted by the three models are very different. The Croton model predicts a broader and only slightly lower sSFR for satellites than centrals at a given stellar mass. In this model, the distribution does not evolve with redshift significantly. The reason for this similarity is that this model adopts a similar treatment for radiative cooling in satellite galaxies as for central galaxies. As we described earlier, the Croton model does not instantaneously strip all the hot gas from subhalos, but allows them to continue to accrete gas from their own hot halo to fuel star formation. For this reason, the majority of the satellite galaxies are star forming and the distribution of satellite galaxies in the sSFR-stellar mass diagram is similar to centrals with slightly reduced star formation rates.

In the Somerville model, the sSFR distribution of satellite galaxies strongly depends on redshift. At $z = 0$, most satellite galaxies are distributed below the dividing line and are quiescent galaxies. At higher redshifts, the sSFR, regardless of stellar mass, is as high as central galaxies

at the same epoch. The distribution of satellite galaxies in the diagram is similar to that of central galaxies.

The Lu model predicts a bimodal distribution of sSFRs. At $z = 0$, the sSFR is low for satellites with mass lower than $\sim 10^{10} M_\odot$, and it jumps to higher values when the stellar mass is higher than $10^{10} M_\odot$. According to the dividing line, low-mass satellites are quiescent and high-mass satellites are star forming. At higher redshifts, the satellite galaxies still have a similar bimodal distribution in their sSFRs. The transition stellar mass, however, decreases with increasing redshift. At $z = 3$ the transition stellar mass is $\sim 10^9 M_\odot$.

In Figure 6 we integrate the star formation rate from galaxies with stellar masses larger than $10^8 M_\odot$ at each redshift to plot the cosmic star formation rate density as a function of redshift. Again, although the three models have different sSFR-stellar mass distributions in detail, they produce similar trends for the volume averaged star formation rate density. The Lu model predicts a large variation at all redshifts for the kinds of acceptable his-

tories, while the two other models fall into the 95% posterior region of the Lu model prediction. This indicates that all three models are consistent with each other, even though they adopt different parameterizations and parameter values. The comparison shows that while more accurate data is needed at high redshift, better measurements of the volume averaged cosmic star formation rate density do not provide enough constraining power to discriminate between the models and to break model degeneracies. However, the comparisons show that detailed observational data, such as the evolution of the star forming sequence and the quiescent fractions at different redshifts, can strongly constrain galaxy formation models. We expect that these data from CANDELS will be helpful to discriminate between the existing models.

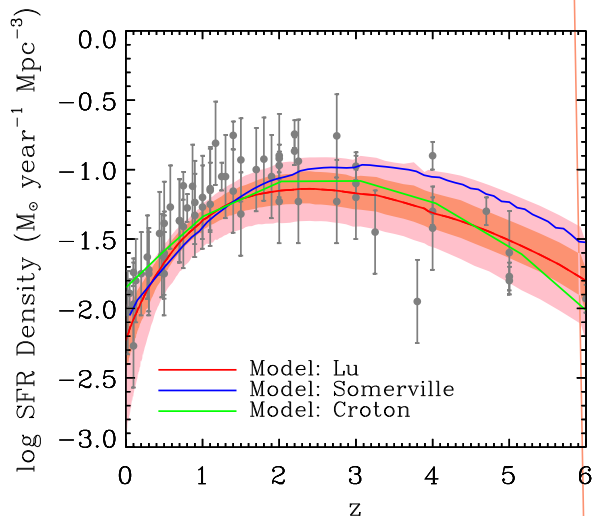


FIG. 6.— Star formation rate density of the universe as a function of redshift. The green line denotes the prediction of the Croton model, the blue line denotes the prediction of the Somerville model, and the dark and light red bands encompass 67% and 95% predictive posterior regions of the Lu model. The data points with error bars are from the compilation of various data sources given in Behroozi et al. (2013b).

4.3. Build-up of stellar mass in central galaxies

To examine the build-up of stellar mass in model galaxies, we keep track of the star formation history of every galaxy along each merger tree. We select central galaxies at $z = 0$ and then calculate their stellar mass-weighted stellar age. In Figure 7 we show the mean relation of the stellar mass-weighted age as a function of stellar mass, for $z = 0$ galaxies predicted by the three models.

We find that all the models predict similar trends for the age–stellar mass relation. The models predict that the stellar mass-weighted age is nearly constant for all stellar masses. The Somerville model predicts that the age of high mass galaxies is slightly higher (0.1 dex) than the two other models, but for galaxies with mass lower than $10^{10} M_{\odot}$, the relation becomes flat, with an age of approximately 8×10^9 yr.

The observational estimates of Gallazzi et al. (2005) indicate that the light-weighted stellar age decreases rapidly with decreasing galaxy stellar mass, from ~ 9 Gyr to ~ 1 Gyr, in contrast to the behavior of all three

models. This is, in general, a much younger stellar population than the models predict, except for the highest mass galaxies. To understand the discrepancy we have done further tests. First, the gray line in Figure 7 shows the averaged stellar mass-weighted age from the empirical model of Behroozi et al. (2013b), which also fits the stellar mass functions of galaxies up to $z = 8$, but is free of the more complex details and parameterizations of galaxy formation modeling. Their results are consistent with that of the SAMs (but not the “fossil” data). Second, including the BC03 stellar population synthesis model, we use the Somerville model to predict the V-band light-weighted age as a function of stellar mass, plotted in light blue. The light-weighted stellar ages are about 0.15 dex lower than the stellar mass-weighted ages. However, this difference cannot explain the large offset between the model predictions and the data. These tests suggest that there may be unaccounted for degeneracies between the stellar age and mass measurements, or that the stellar age estimates may be biased. It may even highlight a deeper problem in reproducing the star formation histories of low-mass galaxies in the SAMs and empirical models.

The light-weighted stellar ages of Gallazzi et al. (2005) were derived from Balmer-line indices, which are sensitive to stellar age (Worthey 1994; Worthey & Ottaviani 1997). However, such indices are very sensitive to recent star formation, which can strongly bias the inferred values. Trager & Somerville (2009) carried out tests, which coupled a SAM to stellar population models to produce synthetic spectra, and computed line strengths from these spectra. They then used the line strengths to determine ages in the same way as for observed spectra and found that the simple stellar population equivalent ages determined by the Balmer-line indices were always younger than mass-weighted ages by more than 40 per cent on average, and younger than light-weighted ages by roughly 25 per cent on average. As shown schematically by Trager et al. (2000b) and quantitatively by Serra & Trager (2007), the addition of a small fraction of young stars to an old population strongly biases the apparent age of a galaxy. This is because hot, young stars contribute much more strongly per unit mass to the Balmer lines than do old stars (Trager et al. 2000a; Serra & Trager 2007). Our results are consistent with such trends, and highlight the importance of considering more complex and realistic star formation histories in computing line-strength-derived ages.

To further explore how central galaxies build up their mass in the models, we select halos of a given virial mass at various redshifts and study how stellar mass and star formation rate in such halos change. First, we consider central galaxy mass as a function of halo mass at redshift $z = 0$ and 2 (Figure 8). We compare the three SAM predictions (solid lines) with the empirically derived results of Behroozi et al. (2013b). At $z = 0$ (left panel) the models agree with each other for halo mass larger than $10^{12} M_{\odot}$, but the Croton model predicts a higher stellar mass-halo mass ratio for high-mass halos. At $M_{\text{vir}} = 10^{14} M_{\odot}$, the mass ratio predicted by the Croton model is about a factor of two higher than other models. At halo masses lower than $10^{12} M_{\odot}$, the models diverge from each other, which is directly related to the

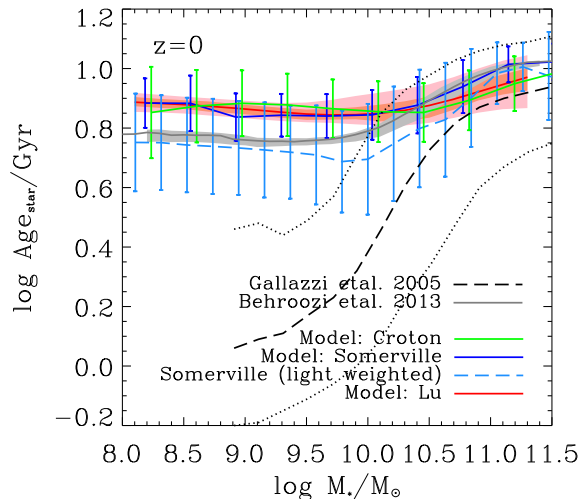


FIG. 7.— Stellar age as a function of stellar mass at $z = 0$ predicted by the three models. The green line denotes the prediction of the Croton model, the blue line denotes the prediction of the Somerville model, and the error bars on them show $1\text{-}\sigma$ scatter of the model galaxy samples. The dark and light red bands encompass 67% and 95% predictive posterior regions of the Lu model. All three of those predictions are stellar mass-weighted stellar ages. The dashed blue line shows the V-band light-weighted stellar ages predicted by the Somerville model. The grey solid line shows the stellar mass-weighted ages of the Behroozi model. The dashed black line is the observational estimates of Gallazzi et al. (2005) and dotted lines are the standard deviations of the observational estimates.

difference in the low-mass end of the predicted stellar mass functions. The Lu model produces the lowest stellar mass function at the low-mass end and, therefore, it produces the lowest stellar mass-halo mass ratio. On the other hand, the Croton model, which shows the steepest low-mass end for the stellar mass function, produces the highest stellar mass halo mass ratio.

More interestingly, the models show similar evolution with redshift between $z = 0$ and 2 but systematically differ from the results of the empirical model, as seen by comparing with the right panel in Figure 8. In the empirical model, the evolution of the stellar mass ratio for high-mass halos is very mild. In contrast, all SAMs, especially the Croton model, predict a relatively stronger evolution, in the sense that high-mass halos build up their stellar mass fairly late. At the low-mass end, the empirical model results suggest that the stellar mass ratio has evolved a lot since $z = 2$, while the SAMs predict a relatively slower evolution. This again shows that, in SAMs, low-mass halos grow their stellar mass at early times more rapidly than they do in such empirical models, and high-mass halos grow their stellar mass more slowly at high redshift.

We now focus our investigation on four halo mass bins, $M_{\text{vir}} = 10^{11}, 10^{12}, 10^{13}$, and $10^{14} M_{\odot}$, with a ± 0.1 dex width, and select central galaxies hosted by such halos at each epoch. In Figure 9 we plot the median central galaxy mass vs. redshift for each SAM (colored solid lines with error bars), separated into these halo mass bins. Also included are the empirical results of Behroozi et al. (2013b) (black line with gray shaded region).

We find that, while the SAM results agree with each other in a broad sense, they disagree with each

other in detail, and also show discrepancies with the Behroozi et al. (2013b) empirical model. For low-mass halos ($10^{11} M_{\odot}$) in the top left panel of Figure 9, the Lu model predicts a mildly decreasing stellar mass with decreasing redshift, the Somerville model predicts a roughly constant stellar mass over all redshifts, and the Croton model predicts a strongly increasing trend with decreasing redshift for $z > 2$ and flat for $z < 2$. In contrast, the Behroozi result suggests a minimum in the characteristic stellar mass hosted in $10^{11} M_{\odot}$ halos at $z \sim 2-3$, and the SFR increases mildly at earlier and later times. In higher mass bins the three SAMs tend to display better agreement with each other across all redshifts plotted, but they uniformly have lower characteristic stellar masses when compared to the Behroozi empirical model.

We also compare the star formation rates in central galaxies for the same halo mass binning and redshift ranges, as shown in four panels in Figure 10. The same plotting schema as used in Figure 9 has been adopted. Here, all models are consistent, although the Somerville SAM displays a larger SFR dispersion at later times (typically $z < 2$) than the other models. This is because the quenching of star formation due to AGN feedback is not explicitly tied to the halo mass in the Somerville model, while in the Croton model and Lu model, halo mass enters explicitly in the recipe for quenching. As a result, in halos near the ‘transition’ mass ($10^{12}-10^{13} M_{\odot}$), some galaxies are quenched, and some are still on the star forming main sequence, leading to a very broad range of SFR at a given halo mass, in spite of the tighter connection between halo mass and stellar mass.

4.4. Build-up of cold gas in central galaxies

Another important aspect of galaxy evolution, especially at high redshift, is the cold gas content. SAMs make explicit predictions for gas in galaxies, as has been recently studied with other models (Power et al. 2010; Fu et al. 2010; Lagos et al. 2011; Popping et al. 2013; Lu et al. 2013). Cold gas is a key component of the modeling process because it is the fuel for star formation and is sensitively affected by various key feedback processes.

For the local galaxy population, there are existing observations that directly probe the cold gas in galaxies (Zwaan et al. 2003, 2005; Giovanelli et al. 2005; Keres et al. 2003). At high redshift, indirect estimates can be obtained based on knowledge of the relationship between star formation and cold gas obtained from local galaxies (e.g. Kennicutt 1998). In this way, one can infer the cold gas content from the observed star formation surface density in high redshift galaxies (Erb et al. 2006; Popping et al. 2012). Therefore, it is important to understand how the cold gas content is predicted in SAMs. The cold gas fraction in galaxies is dichotomous: quiescent galaxies are generally gas poor and elliptical, while star forming galaxies are relatively gas rich and disk dominated (e.g. Martig et al. 2009). We therefore select model galaxies based on their bulge mass to total stellar mass ratio, $B/T \equiv M_{*,B}/(M_{*,B} + M_{*,D})$, where $M_{*,B}$ is the bulge stellar mass, and $M_{*,D}$ is the disk stellar mass. We only select disk dominated galaxies with $B/T < 0.3$ to be analyzed in this section.

In Figure 11, we show the cold gas fraction of disk dominated galaxies, defined as $f_{\text{cold}} = M_{\text{cold}}/(M_{\text{cold}} + M_{*})$, as a function of stellar mass at $z = 0, 1, 2$, and 3. While

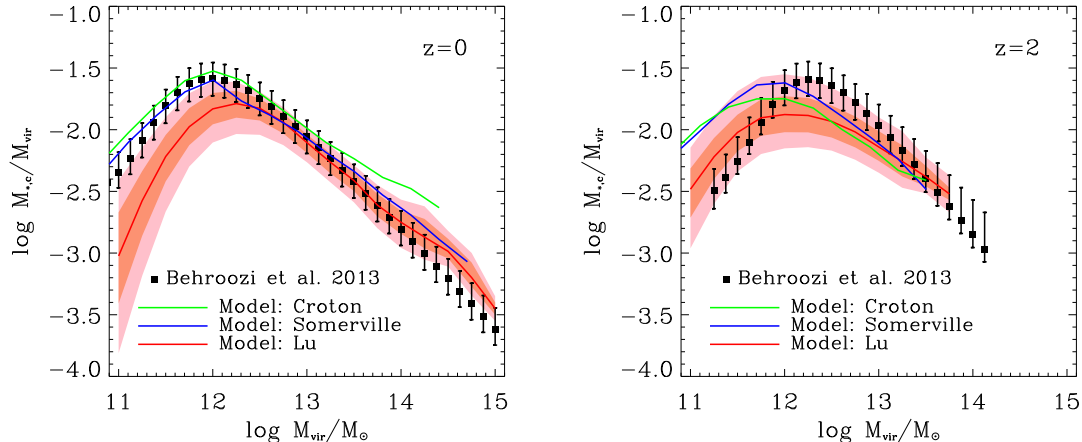


FIG. 8.— The ratio between the central galaxy stellar mass and the host halo virial mass as a function of halo virial mass at $z=0$ and 2. The green line denotes the prediction of the Croton model, the blue line denotes the prediction of the Somerville model, and the dark and light red bands encompass 67% and 95% predictive posterior regions of the Lu model. The black squares with error bars are the empirical constraints derived by Behroozi et al. (2013b).

there are differences in the $f_{\text{cold}} - M_*$ predictions between each of the models, in general, the cold gas fraction decreases with increasing stellar mass. At $z = 0$, all models predict that low mass disk galaxies are dominated by cold gas, with gas fractions commonly reaching above 60%. At higher masses, above $10^{9.5} M_{\odot}$, the majority of the model galaxies have much lower gas fractions, less than 30%, even when classified as disk galaxies. At higher redshifts, the cold gas fraction tends to have larger values at a given stellar mass for all models, especially the high-mass end.

There are also some differences between the models. At all four redshifts, the Croton model predicts a higher cold gas mass fraction than the two other models, and the median predictions of the Lu model are similar to the Somerville model with a slightly lower fraction ($< 10\%$) at very low mass end ($< 10^9 M_{\odot}$). At higher redshift, $z \geq 1$, the Lu model predicts a flatter cold gas mass fraction as a function of stellar mass. The Croton model and the Somerville model have a steeper cold gas mass fraction-stellar mass relation below $10^9 M_{\odot}$. The posterior prediction of the Lu model covers a large range of cold gas fractions. The two other models are always encompassed by the 95% confidence range.

In Figure 11, we also compare the model predictions with observational measurements of the cold gas fraction for local galaxies and an indirect determination of the gas fraction by Popping et al. (2012) for $z \leq 2$. For $z = 0$, we have included compilations of the cold gas fraction from Baldry et al. (2008), Leroy et al. (2008), and Peeples & Shankar (2011). It is worth noting the data points are from different data sources and measure different components of the cold gas. The data from Leroy et al. (2008) are measurements of both HI and H_2 including a correction for helium. The Baldry et al. (2008) data set include the atomic gas masses derived from the Westerbork HI Survey (Swaters & Balcells 2002; Noordermeer et al. 2005) and the HIPASS catalogue (Meyer et al. 2004; Wong et al. 2006), and the literature compilation of Garnett (2002). These data also include a correction of 1.33 for helium, but do not include the molecular hydrogen gas. The compilation

of Peeples & Shankar (2011) includes the total HI gas masses measured from 21 cm line fluxes (McGaugh 2005), the HI gas masses from West et al. (2009, 2010), and the total cold gas measurements from Leroy et al. (2008). At $z = 0$ all models are in general agreement with the data, but with a tendency to overpredict the gas fraction at the intermediate to high-mass end. At higher redshifts, the Popping et al. (2012) results reveal how the cold gas becomes increasingly dominant. Typical galaxies with stellar mass below $10^{9.5} M_{\odot}$ at $z = 1$, and $10^{10.5} M_{\odot}$ at $z = 2$ have more than 95% of their cold baryon mass in cold gas. In the models, however, although the cold gas fraction does increase with redshift, the amplitude is still significantly lower than the data. The large differences between the models and the broad posterior predictive distribution from the constrained Lu model indicate that the prediction of the cold baryon fraction is sensitive to the parameterizations of star formation and feedback implemented in a model. The comparison demonstrates that the gas fraction in the models are not strongly constrained, and observational data for the cold baryon fraction will be very useful to tighten the constraint.

4.5. Build-up of metals in central galaxies

For each model galaxy we predict the amount of metals that are locked into stars. In Figure 12, the stellar metallicity of model central galaxies as a function of stellar mass at $z = 0, 1, 2$, and 3 is plotted, where we adopt a recent calibration of the solar metallicity, $Z_{\odot} = 0.0142$ (Asplund et al. 2009). All models predict a trend that the stellar metallicity increases with stellar mass, which is broadly consistent with the observational estimate of Gallazzi et al. (2005). Trager & Somerville (2009) have shown that, unlike the Balmer-line indices which are strongly biased by the presence of young stars, stellar metal-line indices correlate almost perfectly with mass- and light-weighted metallicity (as shown in Serra & Trager 2007), with very small scatter. The equivalent metallicity derived from fitting the metal-line indices with simple stellar population models is therefore a very good tracer of the light- or even mass-weighted metallicity of a galaxy. This explains why the models

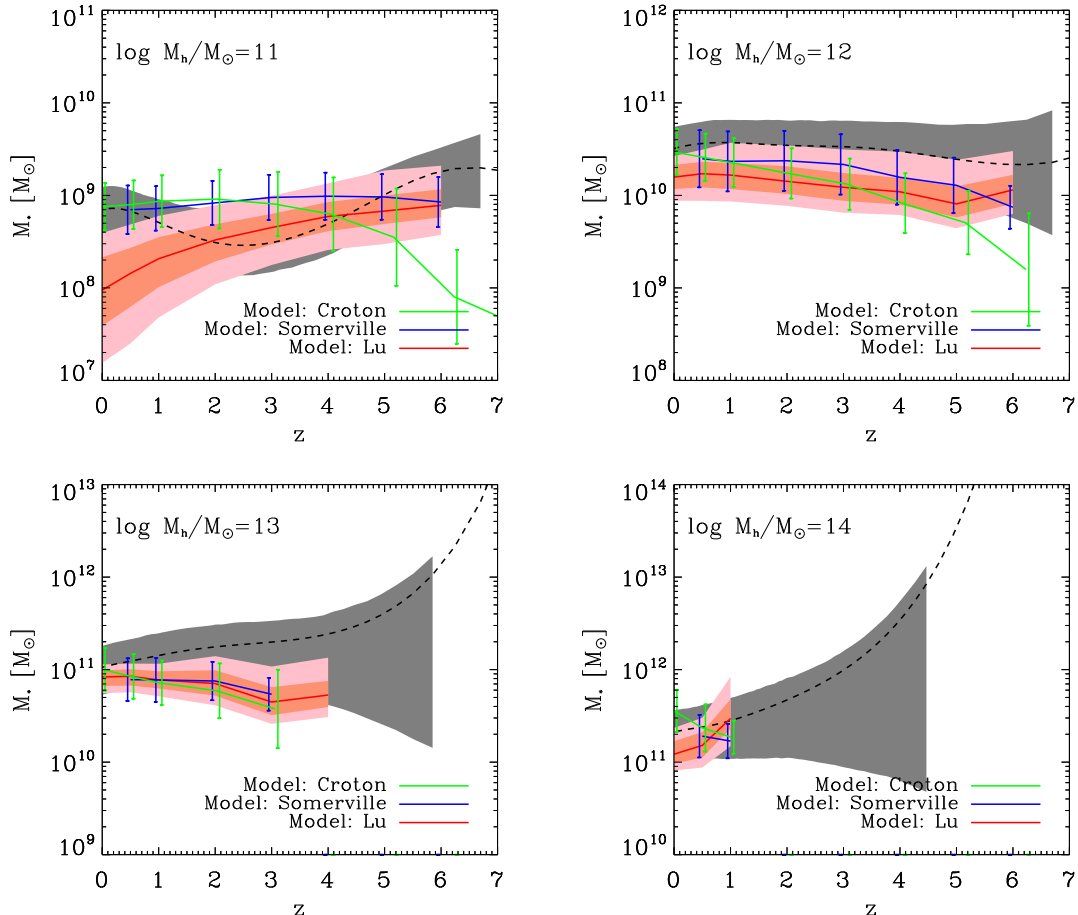


FIG. 9.— Central galaxy stellar mass as a function of redshift for different halo masses. The green line denotes the prediction of the Croton model, the blue line denotes the prediction of the Somerville model, and the error bars on them show the $1\text{-}\sigma$ scatter of the model galaxy samples. The dark and light red bands encompass 67% and 95% predictive posterior regions of the Lu model. The black dashed line and grey band are the results of the empirical model of Behroozi et al. (2013b).

can agree with the metallicity-stellar mass relation of Gallazzi et al. (2005) but seem to be inconsistent with their stellar age-stellar mass relation.

It is clear, however, that the models predict somewhat different slopes for the metallicity-stellar mass relation. The Croton model shows a relatively shallow slope, while the Lu model shows the steepest slope among the three models. The Somerville model matches the data reasonably well. For the high-mass end, $M_* > 10^{10} M_\odot$, the metallicity predicted by the median Lu model is about 0.2-0.3 dex higher than the observation of Gallazzi et al. (2005). At lower masses, the Lu model predicts a rapidly decreasing trend for decreasing stellar masses.

We extrapolate the results of Kirby et al. (2011) from dwarf galaxies to compare with our model predictions. It is clear that the Lu model underpredicts the metallicity for low-mass galaxies. In contrast, the Croton model overpredicts the metallicity in the stellar mass range $10^8 - 10^9 M_\odot$. For higher redshifts, the metallicity-stellar mass relation predicted by the three models barely evolves with time. This is consistent with observational measurements of stellar metallicity for a sample of galaxies at $z \sim 3$ by Sommariva et al. (2012). As a result of the weak redshift evolution, the model predictions at high redshifts keep the same trend, in that the

Croton model consistently predicts the shallowest stellar metallicity-stellar mass relation and the Lu model has the steepest relation.

The discrepancy between the models sheds light on the metal enrichment processes in galaxy formation. As we described earlier, each model assumes a different mass-loading factor for low-mass galaxies in their calibration. The Croton model assumes a constant mass-loading factor, the Somerville model assumes a modest velocity dependence for the loading factor, and the Lu model adopts extremely strong velocity dependence for the mass-loading factor. As a result, the stronger galactic wind in low-mass galaxies in the Lu model tends to blow out a larger amount of metal-enriched cold gas. This explains the trend that, at all redshifts, the Lu model predicts the steepest metallicity-stellar mass relation, and the Croton model predicts the shallowest.

We also make predictions for the gas phase metallicity. Figure 13 shows the metallicity of cold gas for model galaxies as a function of stellar mass at four redshifts, $z = 0, 1, 2,$ and 3 , using the same schema employed previously. To compare our predicted metallicities with observational data, we normalize the predicted metallicities by the solar metallicity, $[12 + \log(\text{O}/\text{H})]_\odot = 8.69$ (Allende Prieto et al. 2001)

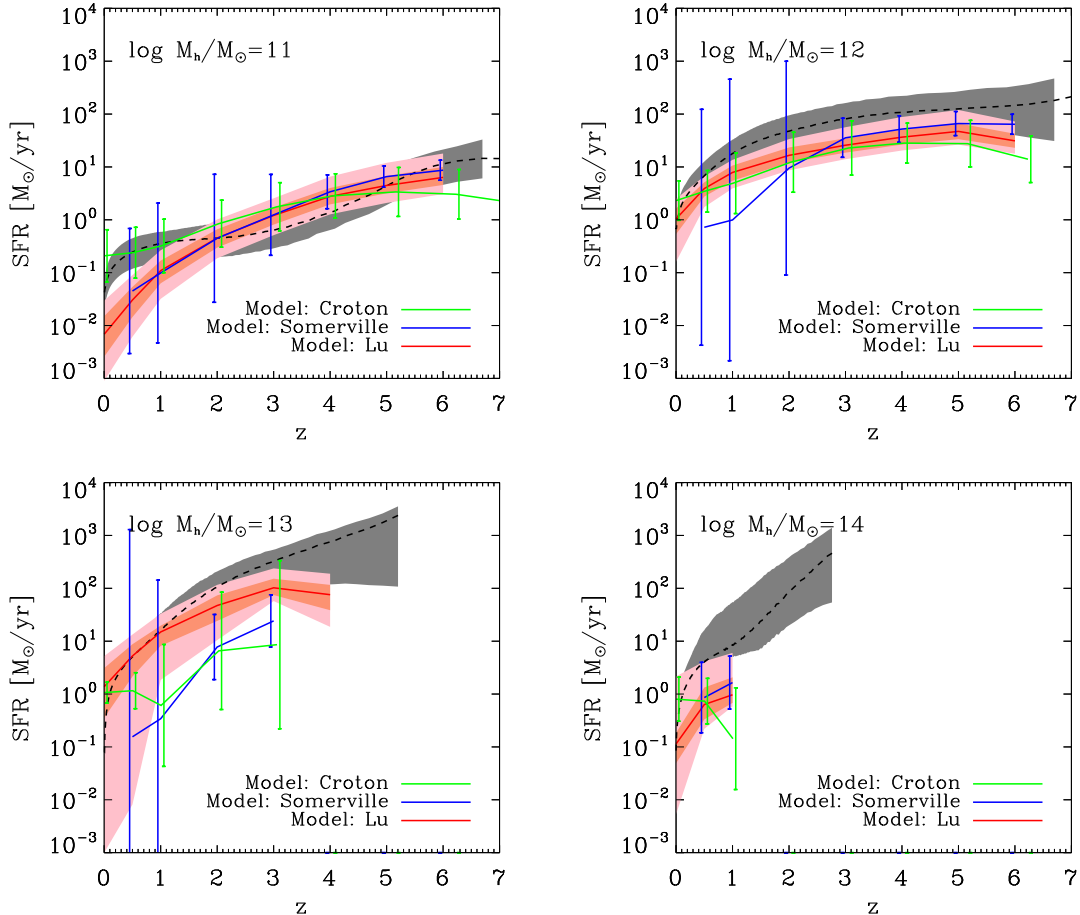


FIG. 10.— Central galaxy star formation rate as a function of redshift for different halo masses. The green line denotes the prediction of the Croton model, the blue line denotes the prediction of the Somerville model, and the error bars on them show the $1\text{-}\sigma$ scatter of the model galaxy samples. The dark and light red bands encompass 67% and 95% predictive posterior regions of the Lu model. The black dashed line and grey band are the results of the empirical model of Behroozi et al. (2013b).

and $Z_{\odot} = 0.0142$ (Asplund et al. 2009)¹¹. The cold gas in SAMs represents the ISM for disc galaxies. Thus, we take only central galaxies with bulge masses less than 0.3 of the total stellar mass. A number of observations are overplotted to be compared with the models: Tremonti et al. (2004) and Andrews & Martini (2013) locally, Savaglio et al. (2005) at $z \sim 0.7$, Erb et al. (2006) at $z \sim 2.2$, and Maiolino et al. (2008) at $z \sim 3 - 4$ (also see Mannucci et al. 2009).

At all redshifts, Figure 13 shows an increasing trend of metallicity with stellar mass for all three models. However, as was the case for the stellar metallicity, we find different slopes and different evolution from the present to $z = 3$. In particular, the Croton model predicts a shallower slope for the gas phase metallicity - stellar mass relation at all epochs, and the Lu model predicts the steepest. At $z > 0$, the Lu model and the Somerville model display very similar results.

Comparing models to data, we find that the Lu and Somerville models lie significantly under the observed relations for all but the highest mass galaxies at $z \leq 1$,

¹¹ Note that our models only track the total metallicity, and do not actually track the Oxygen abundance. We are effectively assuming that all galaxies have solar abundance ratios.

while the shallower slope of the relation in the Croton model is in better agreement with the low redshift observations, especially the recent observational results of Andrews & Martini (2013). However, at higher redshifts all models produce ISM metallicities that are higher than the observational estimates, and significantly so at $z = 3$. It is worth noting that observations of the metallicities of high-redshift galaxies have significant disagreement. For example, Richard et al. (2011) found a weaker redshift evolution in the stellar mass-metallicity relation in a gravitationally lensed galaxy sample at $z \sim 2 - 3$. The authors found that their samples are ~ 0.25 dex more metal-rich than those studied in Maiolino et al. (2008) and Mannucci et al. (2009). Moreover, Mannucci et al. (2010) showed that the cold gas metallicity also depends on SFR using local and $z \sim 2.5$ galaxies. The observed evolution of the metallicity-stellar mass relation could be due to the fact that the SFR for galaxies with a given stellar mass is increasing with redshift. A selection effect, that high SFR galaxies tend to be selected in the high redshift samples, could also result in the metallicities being biased low.

As we discussed earlier, the different mass-loading factor scaling relations adopted in the models strongly affect the resulting metal content of model galaxies. On the

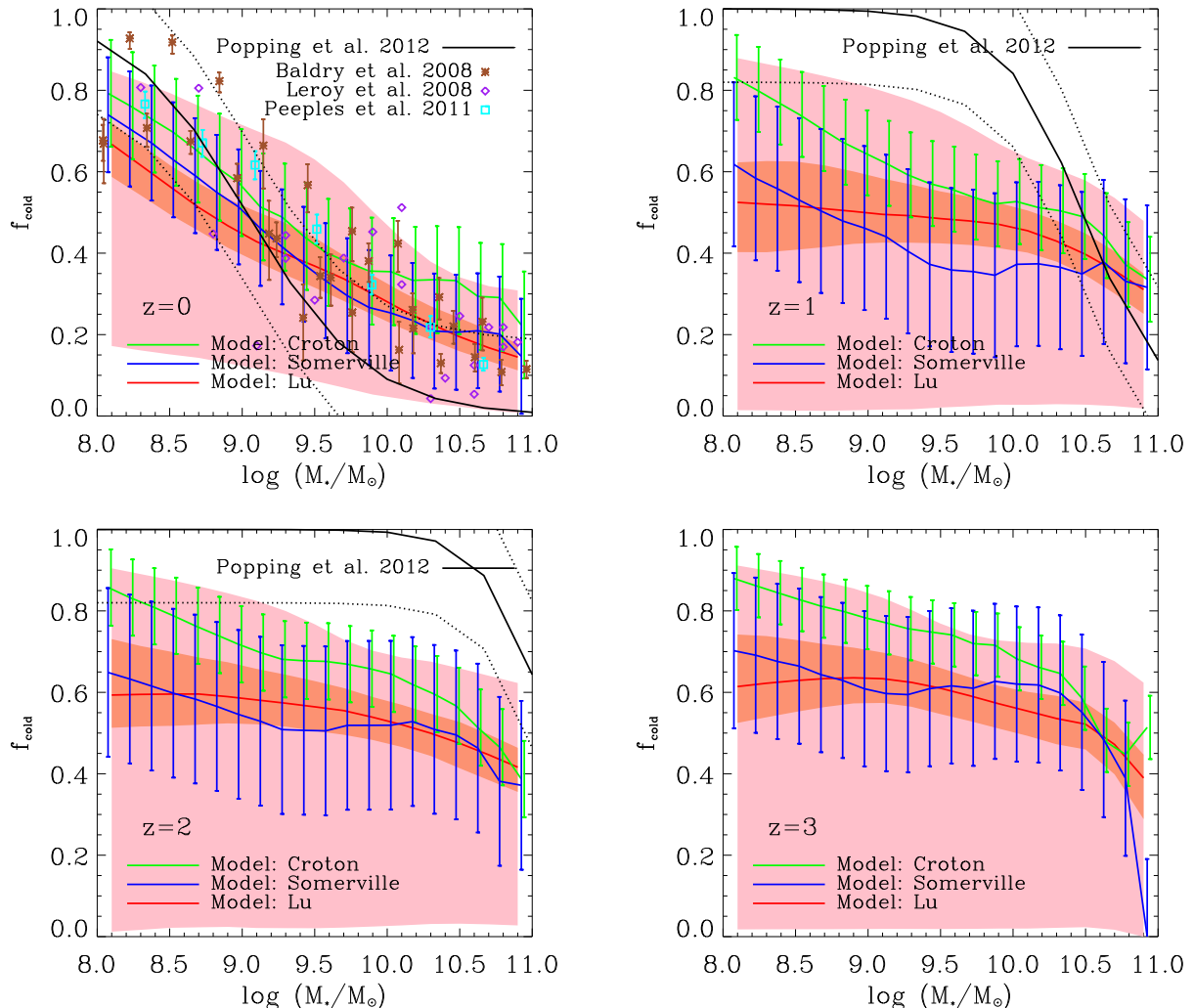


FIG. 11.— Cold gas mass fraction, $f_{\text{cold}} = M_{\text{cold}}/(M_{\text{cold}} + M_*)$, as a function of stellar mass for central disk galaxies at $z = 0, 1, 2$, and 3. The green line denotes the prediction of the Croton model, the blue line denotes the prediction of the Somerville model, and the error bars on them show the $1-\sigma$ scatter of the model galaxy samples. The dark and light red bands show 67% and 95% predictive posterior regions of the Lu model. The black solid line and dotted lines show the indirect empirical estimates of Popping et al. (2012) and their $1-\sigma$ deviations for $z \leq 2$. The color symbols in the $z = 0$ panel show compilations of cold gas fraction measurements for local galaxies from Baldry et al. (2008), Leroy et al. (2008), and Peebles & Shankar (2011).

other hand, the cold gas mass also affects the gas phase metallicity. As we showed in Section 4.4, all models underpredict the cold gas mass at redshift $z > 0$ with respect to the observations. This means the model galaxies at higher redshift have less cold gas to dilute the metallicity at a fixed stellar mass than the observed galaxy population. At high redshifts, the lack of an evolution in the normalization of the gas phase metallicity-stellar mass relations may simply reflect a lack of evolution in the cold gas fraction in the models. If high- z galaxies indeed have higher gas fraction, for the same metal yield and loss rates, the models could produce lower metallicities if the cold gas mass fraction increases.

4.6. History of galaxy outflow

When star formation occurs, SAMs generally assume that strong outflows are generated by star formation feedback. Star formation feedback plays an important role in shaping the low-mass end of the stellar mass func-

tion by blowing out cold gas from the disk that would otherwise be available to form the next generation of stars. Furthermore, supernovae that drive outflows additionally pollute the ISM, ICM and IGM with metals that alter the subsequent cooling rate of gas back into the galactic disk.

In Figure 14 we plot the outflow rate (OFR) predicted by the three models as a function of galaxy stellar mass at different redshifts, $z = 0, 1, 2$ and 3. The model predictions are very different. For the Croton model, the outflow rate is basically linearly proportional to the stellar mass, the reason being that the assumed outflow rate is proportional to SFR, which is roughly proportional to stellar mass. In this model, one finds that as the star formation rate increases rapidly with redshift and stellar mass, the outflow rate for high- z massive galaxies can reach more than $100 M_{\odot}/\text{yr}$.

For the Somerville model, the outflow rate is similar to the Croton model but increases with stellar mass more

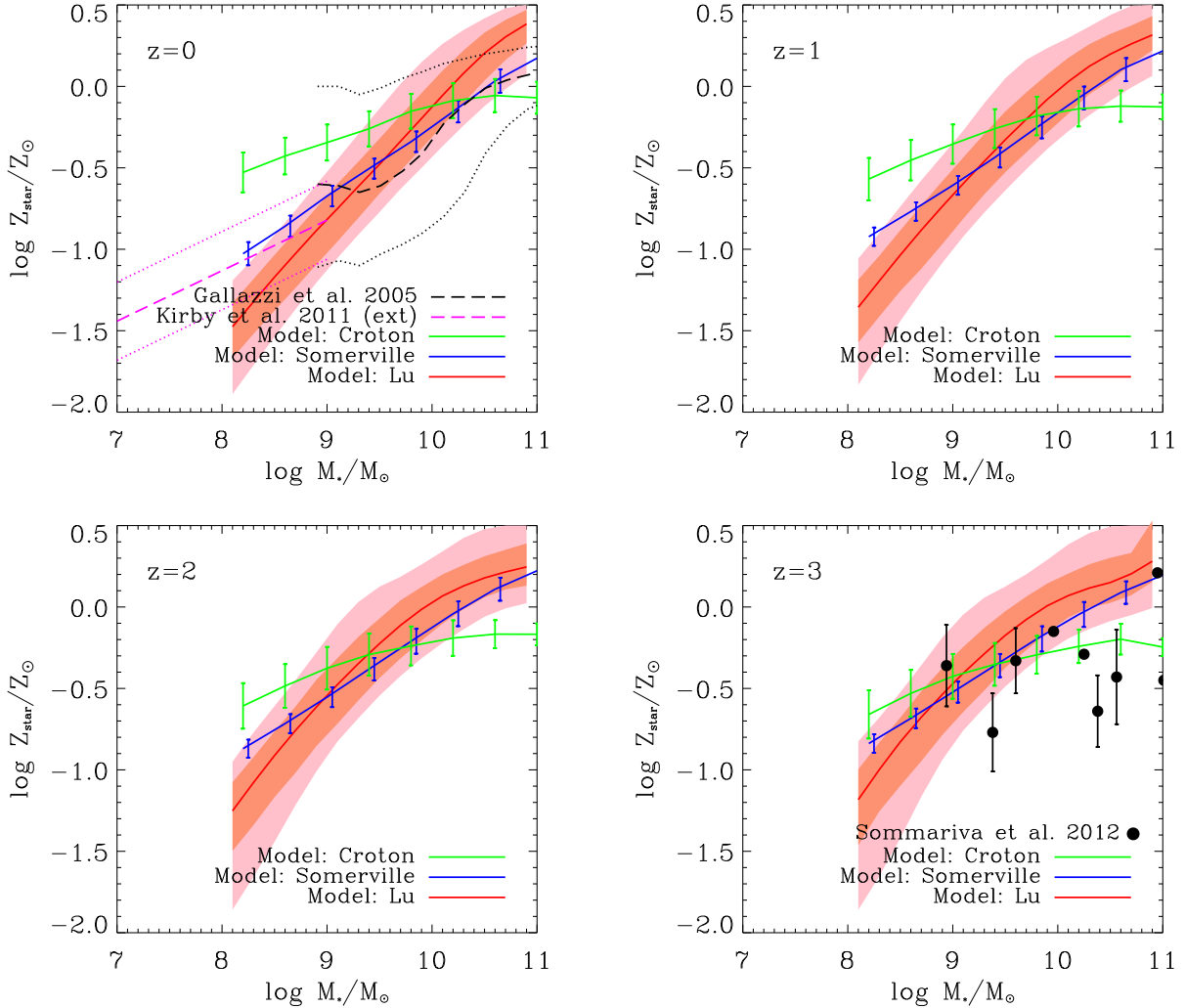


FIG. 12.— Stellar metallicity as a function of stellar mass at $z = 0, 1, 2,$ and 3 predicted by the three SAMs. The green line denotes the prediction of the Croton model, the blue line denotes the prediction of the Somerville model, and the error bars on them show the $1\text{-}\sigma$ scatter of the model galaxy samples. The dark and light red bands encompass 67% and 95% predictive posterior regions of the Lu model. The black dashed line shows the observational estimates of Gallazzi et al. (2005) for local galaxies. The solid magenta line shows the extrapolation of the results of Kirby et al. (2011) to higher stellar masses. The dotted lines are $1\text{-}\sigma$ dispersions of the observational estimates. The black dots in the $z = 3$ panel denote the observational measurements of the stellar metallicity of a sample of galaxies at $z \sim 3$ presented in Sommariva et al. (2012).

slowly. At the low-mass end, the outflow rate is proportional to the stellar mass roughly as $\propto M_*^{2/3}$. This can be understood because outflows in this model are proportional to $\sim SFR/V_{\text{vir}}^2$, and the model is tuned such that $SFR \propto M_*$ and $M_* \propto M_{\text{vir}}^2 \propto V_{\text{vir}}^6$ for low mass galaxies. At the high-mass end, the outflow rate starts to flatten out and even drop due the fact that star formation is quenched.

The Lu model predicts a very different trend for how the outflow rate scales with galaxy mass, and the predictive distribution is very broad. For low-mass galaxies the outflow rate is almost constant, with a weak stellar mass dependence. This is because the dominant mode of the posterior has $OFR \propto SFR/V_{\text{vir}}^6$, resulting in $M_* \propto M_{\text{vir}}^2 \propto V_{\text{vir}}^6$ and $SFR \propto M_*$ for low-mass galaxies and an OFR that is nearly constant. When stellar mass becomes large enough, the outflow rate decreases with increasing stellar mass rapidly because of the strong halo

circular velocity dependence of the OFR. At higher redshifts, this characteristic OFR decrease moves to lower stellar masses. Because the other two models assume a much shallower circular velocity dependence for the OFR, they have steeper slopes. The different predictions for the OFRs show how they can sensitively depend on the model assumptions, and we expect observations of galaxy OFRs and how they scale with galaxy mass could distinguish between such models. Recent hydrodynamical simulations (Puchwein & Springel 2013; Davé et al. 2013) have also found that a steeper circular velocity dependence for the mass-loading factor tends to produce a shallower stellar mass function in the low-mass end. It would be interesting to compare the SAM predicted OFR with the simulation predictions. Our results also suggest that accurate observational data for the faint-end slope of the galaxy mass function and OFR are crucial to constraining feedback models.

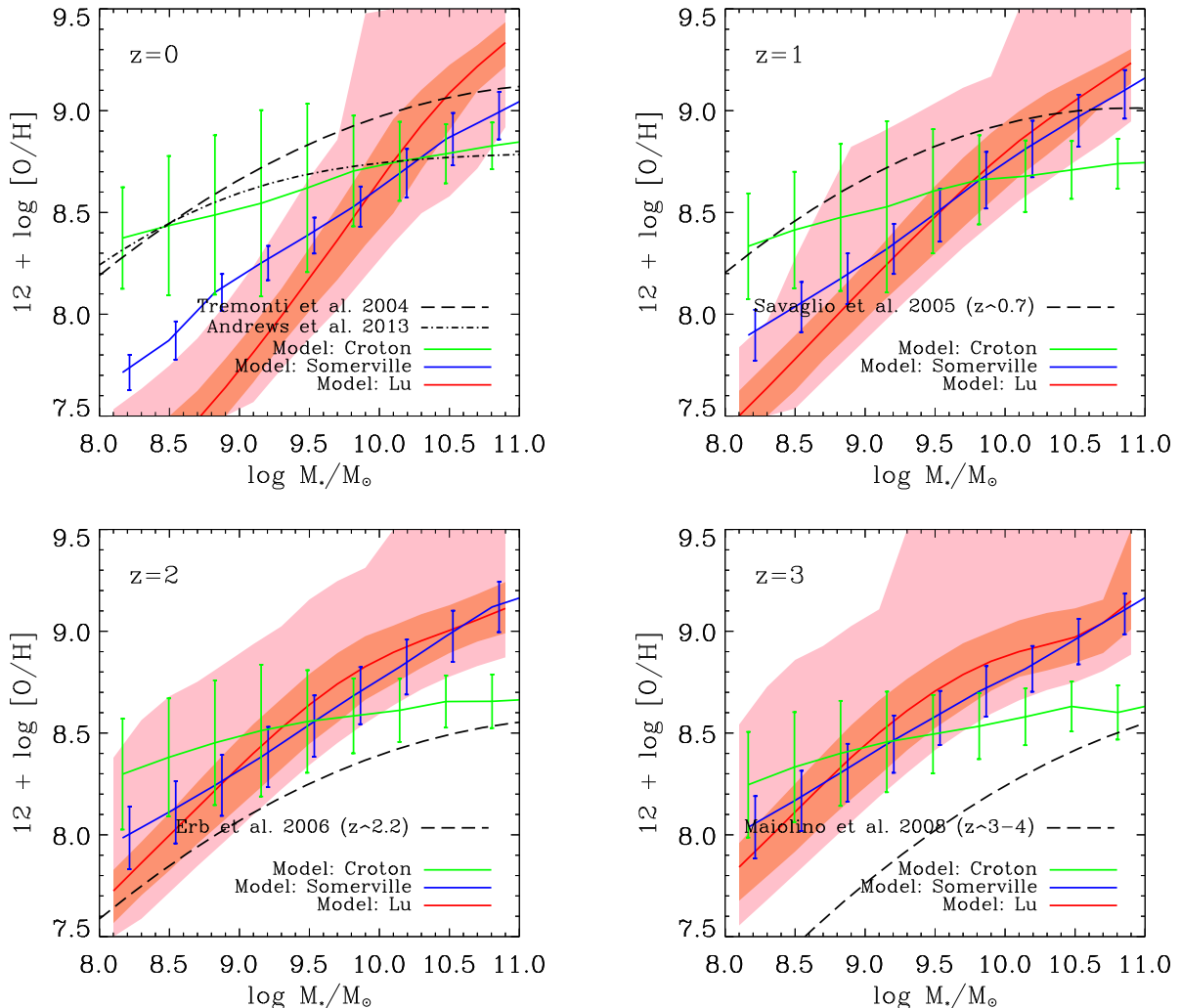


FIG. 13.— ISM metallicity as a function of stellar mass at $z = 0, 1, 2$, and 3 predicted by the SAMs. The green line denotes the prediction of the Croton model, the blue line denotes the prediction of the Somerville model, and the error bars on them show the $1\text{-}\sigma$ scatter of the model galaxy samples. The dark and light red bands encompass 67% and 95% predictive posterior regions of the Lu model. The black dashed lines in each panel are the observational results of Tremonti et al. (2004) for $z = 0.07$, Savaglio et al. (2005) for $z = 0.7$, Erb et al. (2006) for $z = 2.2$, and Maiolino et al. (2008) for $z \sim 3 - 4$.

5. DISCUSSION AND CONCLUSION

We have used three independently developed semi-analytic models (SAMs), the Croton model, which is similar to the one presented in Croton et al. (2006), the Somerville model similar to the one presented in Somerville et al. (2008), and the Lu model updated from Lu et al. (2011b). Each model has been run on the same set of merger trees extracted from the Bolshoi simulation (Klypin et al. 2011). After carefully tuning the models against the stellar mass function of local galaxies, we make predictions for the galaxy stellar and cold gas mass evolution, star formation rate history, metallicities, and outflow rates of the model galaxies. We compare the model predictions to understand the impact of the assumptions for star formation and feedback implemented in those models.

Using hand tuning, we find parameter choices for the Croton and Somerville models that fit the local stellar mass function reasonably well after a large number of

trials. Both models, however, still overpredict the low mass number density somewhat, a common problem with such techniques. For the Lu model, we have performed the calibration using MCMC machinery, which allows us to explore the large parameter space under observational data constraints in a systematic way. The MCMC method identifies favored regions in the parameter space, and randomly selects models from those regions to then make predictions for the galaxy population. We have also noticed that, without additional constraints, these favored regions in the Lu model can be significantly off-set from the values of the other SAMs. In particular, the posterior model for SN feedback outflows in the Lu model suggests a very steep halo circular velocity dependence for the outflow mass-loading factor, $OFR/SFR \propto V_{\text{vir}}^{-6}$. This scaling is significantly steeper than what is normally assumed based on energy conserving winds, $\propto V_{\text{vir}}^{-2}$, or momentum conserving winds, $\propto V_{\text{vir}}^{-1}$.

The steep circular velocity dependence suggests that

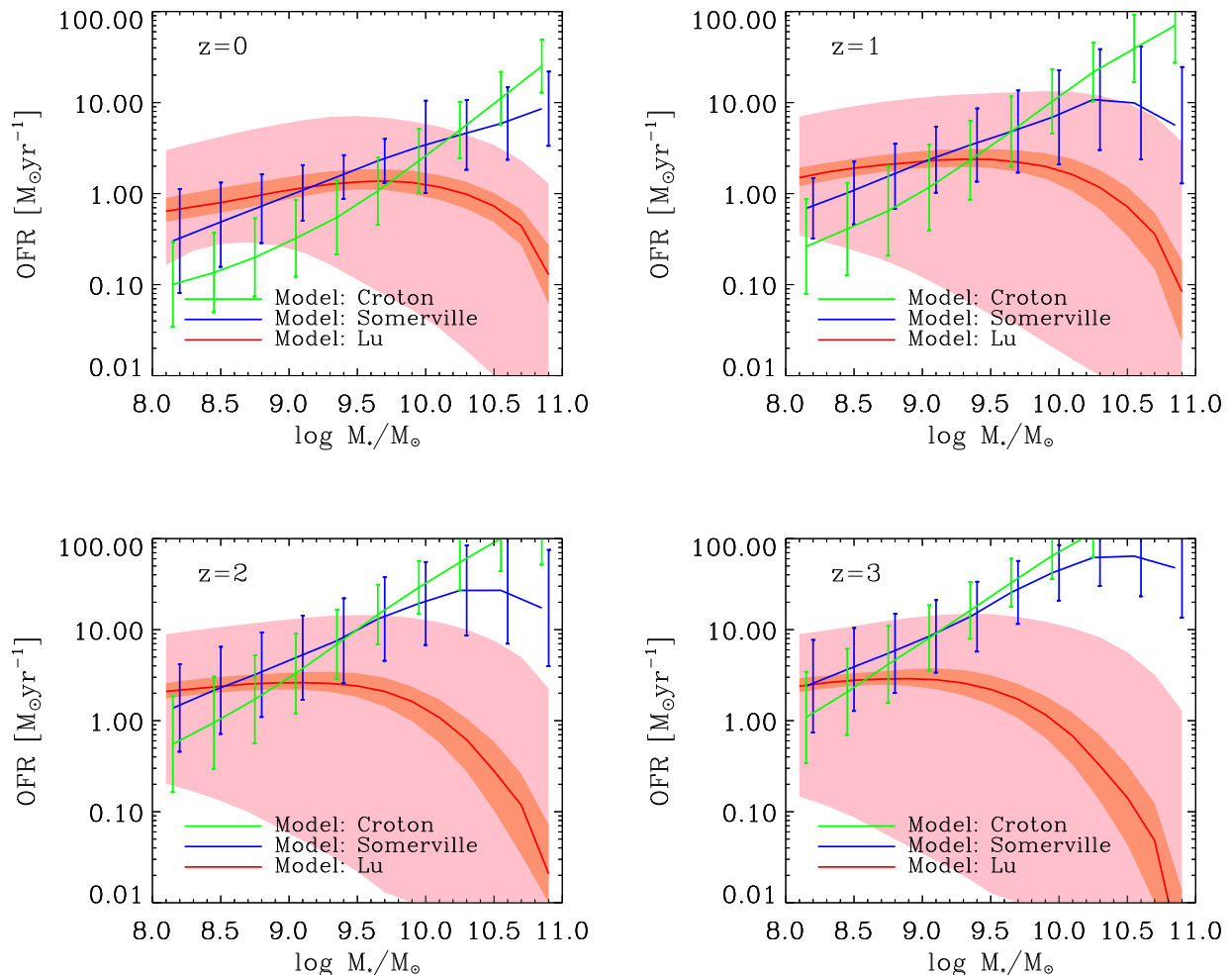


FIG. 14.— Outflow rate of central galaxies as a function of stellar mass predicted by SAMs at $z = 0, 1, 2,$ and 3 . The green line denotes the prediction of the Croton model, the blue line denotes the prediction of the Somerville model, and the error bars on them show the $1\text{-}\sigma$ scatter of the model galaxy samples. The dark and light red bands encompass 67% and 95% predictive posterior regions of the Lu model.

to explain the shallow low-mass slope of the stellar mass function, galaxy formation requires low-mass halos to have very efficient outflows that lead to star formation suppression. Similar indications have been pointed out by other studies. Mutch et al. (2013b) employed a similar MCMC technique to simultaneously reproduce the stellar mass function of galaxies at $z = 0$ and $z \approx 0.8$. The authors found that in order to fit the data at both redshifts, their model had to assume extremely efficient SN feedback in low-mass galaxies. Henriques et al. (2013) constrained their model against both the stellar mass function and B - and K -band luminosity functions over a larger redshift range, and found that to achieve a good fit they needed to assume not only a large mass-loading factor in low mass halos, but also that the timescale for the ejected baryonic mass to reincorporate back into the host halo needed to follow a particular halo mass and redshift dependence, which is different than what is assumed in the three models studied in this paper. It would be interesting to investigate if the extreme circular velocity dependent outflow model used here in

the Lu model and new reincorporation model proposed by Henriques et al. (2013) are essentially similar but just emphasize different processes. It would also be interesting to study what observations can distinguish between these two models.

When we take the locally constrained models and make predictions for the galaxy properties at high redshifts we find that the variance of the model predictions becomes significantly larger at higher redshifts. However, the “best fit” versions of the Croton and the Somerville models are usually encompassed by the 95% range of the posterior predictive distribution of the Lu model. This indicates that, while the SAMs may adopt very different recipes for star formation and feedback, when they are calibrated to the same data in the local universe they agree with each other fairly well in terms of predicting the stellar mass assembly histories of galaxies (at least for the three SAMs considered here). The increasing differences between the model predictions also suggest that more accurate measurements at high- z could be used to discriminate between them and to break some of the de-

generacy between model parameters.

Comparing the model predictions with existing data we have found that even though the SAMs are tuned to match only the local stellar mass function, they generally produce star formation histories that are qualitatively similar to those inferred observationally, but with some discrepancies. In the SAMs considered here, low mass halos tend to form stars more rapidly at high redshift than what is inferred from observations, and their star formation rates are too low at low redshift compared with observations. When we look at the typical ages of stars predicted for local galaxies, we find that low-mass model galaxies are systematically older than those observational estimates. The predictions for the stellar ages in this paper are very similar to those produced by other SAMs (e.g. Fontanot et al. 2009; De Lucia & Borgani 2012), suggesting that this issue is a general one, extending beyond just the three models we compare here. For high-mass halos, the models have difficulty producing high enough star formation rates at early times to match the data. The lack of star formation in high-redshift high-mass halos results in a small underprediction of objects at the high-mass end of the stellar mass function at these redshifts. However, we have found that when a reasonable assumption about the uncertainty in estimating the observed stellar masses is included, the model predictions are in reasonable agreement with the observations at the high-mass end.

The issues of overpredicting the star formation rate at high redshift and underpredicting of the star formation rate at low redshift for low-mass halos are closely related. All three models tend to produce rapid star formation in low-mass halos at early times because gas cooling is efficient, and because halos are denser, with higher circular velocities at a given mass, making supernova feedback less effective as it is currently parameterized. Therefore, in the models, these halos have already formed a large fraction of the expected present day stellar mass at early times. In this situation, to match the stellar mass function of local galaxies, the models have to suppress further star formation. They thus tend to predict rather low star formation rates locally for low-mass systems, which is apparently inconsistent with observations, which show that low mass systems tend to still be star forming. Weinmann et al. (2012) have reported similar behavior in several SAMs as well as several sets of hydrodynamic simulations, and argued that the problem is general, and may be connected with the widely used “sub-grid” recipes for star formation and stellar feedback.

The predictions for gas phase metallicity as a function of stellar mass show a large discrepancy between the three models. For example, the 95% posterior predictive distribution of the Lu model no longer encompasses the two other models. Moreover, the evolutionary trends of the metallicity relations are all very different. The Lu model, which fits the low-mass end of the local stellar mass function better than other models, predicts the steepest metallicity-stellar mass relation. It indicates that the model efficiently ejects metal-enriched mass via

strong feedback. The Croton model, which retains the re-heated gas within the halo, predicts highest metallicity for low-mass galaxies.

We have found that the differences between the model predictions primarily stem from the different parameterizations of star formation feedback, which is invoked to suppress star formation in low-mass halos. This feedback is effectively modeled as outflow of the disk gas. The outflow not only limits the cold baryon mass that is able to fuel future star formation, but also blows out the metal-enriched ISM in a galaxy. We have found that to match the faint-end slope of the stellar mass function, the outflow rate is required to be as high as about $1 M_{\odot} \text{ yr}^{-1}$ for low-mass galaxies, but such a high outflow rate results in metallicity-stellar mass relations that are much steeper than current observational estimates. The tension between the match of the stellar mass function and the mismatch of the metallicity-stellar mass relation strongly suggests that star formation feedback is not properly modeled in these current models of galaxy formation.

Among the observables we have compared, we have found that metallicities and outflow rates show the largest discrepancies between models. The fraction of galaxies that are quiescent is also highly discrepant. Not only does each model predict a different trend for those quantities as functions of stellar mass, but the variation within one model family is large. This indicates that the observational data for those quantities have strong power for further constraining the uncertainties of galaxy formation models. The CANDELS survey, which has just finished taking data, will provide a unique testbed for these models. In particular, the survey will allow a self consistent and comprehensive study of the star formation rates, stellar masses, metallicities, and AGN fractions of galaxies from $z \sim 1$ back to the reionization epoch, and the environmental dependences of these properties. This study provides theoretical context for these data, and indicates that matching tighter constraints on, for example, the connection between stellar mass and halo mass at different cosmic epochs, the evolution of the fraction of quiescent and star forming galaxies and the joint evolution of metallicity and stellar mass, will provide insight into the physics of galaxy formation.

DC wishes to acknowledge receipt of a QEII Fellowship by the Australian Research Council. LP, CM and JP have been supported by the STScI CANDELS grant HST-GO-12060.12-A and by NSF-AST-1010033. PB received support from an HST Theory grant (program number HSTAR- 12159.01-A) as well as a Giacconi Fellowship, both provided through grants from the Space Telescope Science Institute, which is operated by the Association of Universities for Research in Astronomy, Incorporated, under NASA contract NAS5-26555. DCK is supported by NSF grant AST-08-08133 and HST grant HST GO-12060.

REFERENCES

Adelman-McCarthy, J. K., et al. 2008, *ApJS*, 175, 297

Allende Prieto, C., Lambert, D. L., & Asplund, M. 2001, *ApJ*, 556, L63

- Andrews, B. H., & Martini, P. 2013, *ApJ*, 765, 140
- Asplund, M., Grevesse, N., Sauval, A. J., & Scott, P. 2009, *ARA&A*, 47, 481
- Baldry, I. K., Glazebrook, K., & Driver, S. P. 2008, *MNRAS*, 388, 945
- Baldry, I. K., et al. 2012, *MNRAS*, 421, 621
- Baugh, C. M. 2006, *Reports on Progress in Physics*, 69, 3101
- Behroozi, P. S., Wechsler, R. H., & Conroy, C. 2013a, *ApJ*, 762, L31
- . 2013b, *ApJ*, 770, 57
- Behroozi, P. S., Wechsler, R. H., & Wu, H.-Y. 2013c, *ApJ*, 762, 109
- Behroozi, P. S., Wechsler, R. H., Wu, H.-Y., Busha, M. T., Klypin, A. A., & Primack, J. R. 2013d, *ApJ*, 763, 18
- Benson, A. J. 2012, *New Astronomy*, 17, 175
- Best, P. N., von der Linden, A., Kauffmann, G., Heckman, T. M., & Kaiser, C. R. 2007, *MNRAS*, 379, 894
- Bigiel, F., Leroy, A., Walter, F., Brinks, E., De Blok, W. J. G., Madore, B., & Thornley, M. D. 2008, *AJ*, 136, 2846
- Binney, J., & Tremaine, S. 1987, *Galactic dynamics* (Princeton, NJ, Princeton University Press, 1987, 747 p.)
- Blanton, M. R., Lupton, R. H., Schlegel, D. J., Strauss, M. a., Brinkmann, J., Fukugita, M., & Loveday, J. 2005, *ApJ*, 631, 208
- Bower, R. G., Benson, A. J., Malbon, R., Helly, J. C., Frenk, C. S., Baugh, C. M., Cole, S., & Lacey, C. G. 2006, *MNRAS*, 370, 645
- Boylan-Kolchin, M., Ma, C., & Quataert, E. 2008, *MNRAS*, 383, 93
- Braak, C. 2006, *Statistics and Computing*, 16, 239
- Brammer, G. B., et al. 2011, *ApJ*, 739, 24
- Bruzual, G., & Charlot, S. 2003, *MNRAS*, 344, 1000
- Caputi, K. I., Cirasuolo, M., Dunlop, J. S., McLure, R. J., Farrah, D., & Almaini, O. 2011, *MNRAS*, 413, 162
- Cattaneo, A., Dekel, A., Devriendt, J., Guiderdoni, B., & Blaizot, J. 2006, *MNRAS*, 370, 1651
- Cattaneo, A., et al. 2007, *MNRAS*, 377, 63
- Chabrier, G. 2003, *PASP*, 115, 763
- Cole, S. 1991, *ApJ*, 367, 45
- Cole, S., Aragón-Salamanca, A., Frenk, C. S., Navarro, J. F., & Zepf, S. E. 1994, *MNRAS*, 271, 781
- Cox, T. J., Dutta, S. N., Di Matteo, T., Hernquist, L., Hopkins, P. F., Robertson, B., & Springel, V. 2006, *ApJ*, 650, 791
- Cox, T. J., Jonsson, P., Somerville, R. S., Primack, J. R., & Dekel, A. 2008, *MNRAS*, 384, 386
- Croton, D. J., et al. 2006, *MNRAS*, 365, 11
- Davé, R., Katz, N., Oppenheimer, B. D., Kollmeier, J. A., & Weinberg, D. H. 2013, *arXiv.org, astro-ph.CO*
- De Lucia, G., & Blaizot, J. 2007, *MNRAS*, 375, 2
- De Lucia, G., & Borgani, S. 2012, *MNRAS*, 426, L61
- De Lucia, G., Boylan-Kolchin, M., Benson, A. J., Fontanot, F., & Monaco, P. 2010, *MNRAS*, 406, 1533
- Dekel, A., et al. 2009, *Nature*, 457, 451
- Dunkley, J., et al. 2009, *ApJS*, 180, 306
- Erb, D. K., Shapley, A. E., Pettini, M., Steidel, C. C., Reddy, N. A., & Adelberger, K. L. 2006, *ApJ*, 644, 813
- Fontanot, F., De Lucia, G., Monaco, P., Somerville, R. S., & Santini, P. 2009, *MNRAS*, 397, 1776
- Fu, J., Guo, Q., Kauffmann, G., & Krumholz, M. R. 2010, *MNRAS*, 409, 515
- Gallazzi, A., Charlot, S., Brinchmann, J., White, S. D. M., & Tremonti, C. A. 2005, *MNRAS*, 362, 41
- Garnett, D. R. 2002, *ApJ*, 581, 1019
- Gelman, A., & Rubin, D. 1992, *Statistical Science*, 7, 457
- Giovanelli, R., et al. 2005, *AJ*, 130, 2598
- Gnedin, N. Y. 2000, *ApJ*, 542, 535
- González, V., Labbé, I., Bouwens, R. J., Illingworth, G., Franx, M., & Kriek, M. 2011, *ApJ*, 735, L34
- Grogin, N. A., et al. 2011, *ApJS*, 197, 35
- Guo, Q., et al. 2011, *MNRAS*, 164
- Henriques, B. M. B., White, S. D. M., Thomas, P. A., Angulo, R. E., Guo, Q., Lemson, G., & Springel, V. 2013, *MNRAS*, 431, 3373
- Hirschmann, M., Somerville, R. S., Naab, T., & Burkert, A. 2012, *MNRAS*, 426, 237
- Hopkins, P. F., Hernquist, L., Cox, T. J., Robertson, B., Di Matteo, T., & Springel, V. 2006, *ApJ*, 639, 700
- Hopkins, P. F., Hernquist, L., Cox, T. J., Robertson, B., & Krause, E. 2007, *ApJ*, 669, 45
- Hopkins, P. F., et al. 2009, *MNRAS*, 397, 802
- Jarosik, N., et al. 2011, *ApJS*, 192, 14
- Kang, X., Jing, Y. P., Mo, H. J., & Börner, G. 2005, *ApJ*, 631, 21
- Kauffmann, G. 1996, *MNRAS*, 281, 475
- Kauffmann, G., Colberg, J. M., Diaferio, A., & White, S. D. M. 1999, *MNRAS*, 303, 188
- Kauffmann, G., Heckman, T. M., & Best, P. N. 2008, *MNRAS*, 384, 953
- Kauffmann, G., White, S. D. M., & Guiderdoni, B. 1993, *MNRAS*, 264, 201
- Kennicutt, Jr., R. C. 1998, *ApJ*, 498, 541
- Kennicutt, R. C. J. 1989, *ApJ*, 344, 685
- Kennicutt, R. C. J., et al. 2007, *ApJ*, 671, 333
- Keres, D., Yun, M. S., & Young, J. S. 2003, *ApJ*, 582, 659
- Kimm, T., et al. 2009, *MNRAS*, 394, 1131
- Kirby, E. N., Lanfranchi, G. A., Simon, J. D., Cohen, J. G., & Guhathakurta, P. 2011, *ApJ*, 727, 78
- Klypin, A. A., Trujillo-Gomez, S., & Primack, J. 2011, *ApJ*, 740, 102
- Koekemoer, A. M., et al. 2011, *ApJS*, 197, 36
- Kollmeier, J. A., et al. 2006, *ApJ*, 648, 128
- Komatsu, E., et al. 2009, *ApJS*, 180, 330
- Kravtsov, A. V., Gnedin, O. Y., & Klypin, A. A. 2004, *ApJ*, 609, 482
- Lagos, C. d. P., Lacey, C. G., Baugh, C. M., Bower, R. G., & Benson, A. J. 2011, *MNRAS*, 416, 1566
- Lee, K.-S., et al. 2012, *ApJ*, 752, 66
- Leroy, A. K., Walter, F., Brinks, E., Bigiel, F., de Blok, W. J. G., Madore, B., & Thornley, M. D. 2008, *AJ*, 136, 2782
- Lu, Y., Kereš, D., Katz, N., Mo, H. J., Fardal, M., & Weinberg, M. D. 2011a, *MNRAS*, 416, 660
- Lu, Y., Mo, H. J., Katz, N., & Weinberg, M. D. 2012, *MNRAS*, 421, 1779
- Lu, Y., Mo, H. J., Lu, Z., Katz, N., & Weinberg, M. D. 2013, *ArXiv e-prints*
- Lu, Y., Mo, H. J., Weinberg, M. D., & Katz, N. 2011b, *MNRAS*, 416, 1949
- Macciò, A. V., Kang, X., Fontanot, F., Somerville, R. S., Kopusov, S., & Monaco, P. 2010, *MNRAS*, 402, 1995
- Maiolino, R., et al. 2008, *A&A*, 488, 463
- Mannucci, F., Cresci, G., Maiolino, R., Marconi, A., & Gnerucci, A. 2010, *MNRAS*, 408, 2115
- Mannucci, F., et al. 2009, *ApJ*, 398, 1915
- Marchesini, D., van Dokkum, P. G., Förster Schreiber, N. M., Franx, M., Labbé, I., & Wuyts, S. 2009, *ApJ*, 701, 1765
- Martig, M., Bournaud, F., Teyssier, R., & Dekel, A. 2009, *ApJ*, 707, 250
- Martin, C. L. 1999, *ApJ*, 513, 156
- McGaugh, S. S. 2005, *ApJ*, 632, 859
- Menci, N., Fontana, A., Giallongo, E., Grazian, A., & Salimbeni, S. 2006, *arXiv.org, astro-ph*
- Meyer, M. J., et al. 2004, *MNRAS*, 350, 1195
- Mo, H. J., Mao, S., & White, S. D. M. 1998, *MNRAS*, 295, 319
- Monaco, P., Fontanot, F., & Taffoni, G. 2007, *MNRAS*, 375, 1189
- Moustakas, J., et al. 2013, *ApJ*, 767, 50
- Mutch, S. J., Croton, D. J., & Poole, G. B. 2013a, *MNRAS*, 435, 2445
- Mutch, S. J., Poole, G. B., & Croton, D. J. 2013b, *MNRAS*, 428, 2001
- Navarro, J. F., Frenk, C. S., & White, S. D. M. 1996, *ApJ*, 462, 563
- Neistein, E., & Weinmann, S. M. 2010, *MNRAS*, 405, 2717
- Noeske, K. G., et al. 2007, *ApJ*, 660, L43
- Noordermeer, E., van der Hulst, J. M., Sancisi, R., Swaters, R. A., & van Albada, T. S. 2005, *A&A*, 442, 137
- Nulsen, P. E. J., & Fabian, A. C. 2000, *MNRAS*, 311, 346
- Peeples, M. S., & Shankar, F. 2011, *MNRAS*, 417, 2962
- Planck Collaboration et al. 2013, *ArXiv e-prints*
- Popping, G., Caputi, K. I., Somerville, R. S., & Trager, S. C. 2012, *MNRAS*, 425, 2386
- Popping, G., Somerville, R. S., & Trager, S. C. 2013, *ArXiv e-prints*
- Power, C., Baugh, C., & Lacey, C. 2010, *MNRAS*, 406, 43
- Prada, F., Klypin, A. A., Cuesta, A. J., Betancort-Rijo, J. E., & Primack, J. 2012, *MNRAS*, 423, 3018

- Puchwein, E., & Springel, V. 2013, MNRAS, 428, 2966
- Richard, J., Jones, T., Ellis, R., Stark, D. P., Livermore, R., & Swinbank, M. 2011, MNRAS, 413, 643
- Robertson, B., Bullock, J. S., Cox, T. J., Di Matteo, T., Hernquist, L., Springel, V., & Yoshida, N. 2006, ApJ, 645, 986
- Salim, S., et al. 2007, ApJS, 173, 267
- Santini, P., et al. 2012, A&A, 538, A33
- Saro, A., Lucia, G. D., Borgani, S., & Dolag, K. 2010, MNRAS, 406, 729
- Savaglio, S., et al. 2005, ApJ, 635, 260
- Schaerer, D., de Barros, S., & Sklias, P. 2013, A&A, 549, A4
- Schaye, J. 2004, ApJ, 609, 667
- Serra, P., & Trager, S. C. 2007, MNRAS, 374, 769
- Shakura, N. I., & Sunyaev, R. A. 1973, A&A, 24, 337
- Somerville, R. S., Gilmore, R. C., Primack, J. R., & Domínguez, A. 2012, MNRAS, 423, 1992
- Somerville, R. S., & Kolatt, T. S. 1999, MNRAS, 305, 1
- Somerville, R. S., & Primack, J. R. 1999, ApJ, 310, 1087
- Somerville, R. S., Primack, J. R., & Faber, S. M. 2001, MNRAS, 320, 504, not yet read, cited for the merger triggered starburst model
- Somerville, R. S., et al. 2008, ApJ, 672, 776
- Sommariva, V., Mannucci, F., Cresci, G., Maiolino, R., Marconi, A., Nagao, T., Baroni, A., & Grazian, A. 2012, A&A, 539, A136
- Spergel, D. N., et al. 2007, ApJS, 170, 377
- Springel, V., White, S. D. M., Tormen, G., & Kauffmann, G. 2001, MNRAS, 328, 726
- Springel, V., et al. 2005, Nature, 435, 629
- Stark, D. P., Schenker, M. A., Ellis, R., Robertson, B., McLure, R., & Dunlop, J. 2013, ApJ, 763, 129
- Sutherland, R. S., & Dopita, M. A. 1993, ApJS, 88, 253
- Swaters, R. A., & Balcells, M. 2002, A&A, 390, 863
- Taylor, J. E., & Babul, A. 2001, ApJ, 559, 716
- Trager, S. C., Faber, S. M., Worthey, G., & González, J. J. 2000a, AJ, 120, 165
- . 2000b, AJ, 119, 1645
- Trager, S. C., & Somerville, R. S. 2009, MNRAS, 395, 608
- Tremonti, C. A., et al. 2004, ApJ, 613, 898
- Vestergaard, M. 2004, ApJ, 601, 676
- Wang, L., Weinmann, S. M., & Neistein, E. 2012, MNRAS, 421, 3450
- Weinmann, S. M., Pasquali, A., Oppenheimer, B. D., Finlator, K., Mendel, J. T., Crain, R. A., & Macciò, A. V. 2012, MNRAS, 426, 2797
- West, A. A., Garcia-Appadoo, D. A., Dalcanton, J. J., Disney, M. J., Rockosi, C. M., & Ivezić, Ž. 2009, AJ, 138, 796
- West, A. A., Garcia-Appadoo, D. A., Dalcanton, J. J., Disney, M. J., Rockosi, C. M., Ivezić, Ž., Bentz, M. C., & Brinkmann, J. 2010, AJ, 139, 315
- White, S. D. M., & Frenk, C. S. 1991, ApJ, 379, 52
- White, S. D. M., & Rees, M. J. 1978, MNRAS, 183, 341
- Wilkins, S. M., Trentham, N., & Hopkins, A. M. 2008, MNRAS, 385, 687
- Wong, O. I., et al. 2006, MNRAS, 371, 1855
- Worthey, G. 1994, ApJS, 95, 107
- Worthey, G., & Ottaviani, D. L. 1997, ApJS, 111, 377
- Yang, X., Mo, H. J., van den Bosch, F. C., Bonaca, A., Li, S., Lu, Y., Lu, Y., & Lu, Z. 2013, ArXiv e-prints
- Zentner, A. R., Kravtsov, A. V., Gnedin, O. Y., & Klypin, A. A. 2005, ApJ, 629, 219
- Zhao, D. H., Jing, Y. P., Mo, H. J., & Börner, G. 2009, ApJ, 707, 354
- Zwaan, M. A., Meyer, M. J., Staveley-Smith, L., & Webster, R. L. 2005, MNRAS, 359, L30
- Zwaan, M. A., et al. 2003, AJ, 125, 2842